Monthly Notices of the ROYAL ASTRONOMICAL SOCIETY

MNRAS **540,** 1107–1123 (2025) https://doi.org/10.1093/mnras/staf749
Advance Access publication 2025 May 08

The unabridged satellite luminosity function of Milky Way-like galaxies in ΛCDM: the contribution of 'orphan' satellites

Isabel M. E. Santos-Santos [1]★ Carlos S. Frenk,[1] Julio F. Navarro,[2] Shaun Cole[1] and John Helly[1]

[1]*Institute for Computational Cosmology, Department of Physics, Durham University, South Road, Durham DH1 3LE, UK*
[2]*Department of Physics and Astronomy, University of Victoria, Victoria, BC V8P 5C2, Canada*

Accepted 2025 April 29. Received 2025 April 14; in original form 2024 October 25

ABSTRACT

We study the abundance, radial distribution, and orbits of luminous satellites in simulations of Milky Way-mass dark haloes in the Λcold dark matter (ΛCDM) cosmology. We follow the evolution of a halo from the Aquarius project and the formation of its 'maximal' satellite population with the GALFORM semi-analytic model of galaxy formation. This population consists of all subhaloes able to form stars through efficient gas cooling before or after reionization, which effectively selects systems with peak circular velocities exceeding a critical threshold of roughly $\sim$ 15–20 km s^{-1}. The total number of luminous satellites is sensitive to the assumed redshift of reionization, but the shape of the GALFORM satellite stellar mass function is robust, peaking at the stellar mass ($\sim 10^3 M_\odot$) of a halo just above the critical threshold. Subhaloes are prone to artificial disruption in the tidal field of the main halo, with the number of surviving satellites increasing with resolution. Even in the highest resolution simulation (Aq-L1, with particle mass $m_p \sim 10^3\,M_\odot$), a substantial number of satellite subhaloes are disrupted, leaving behind 'orphan' galaxies tracked in GALFORM by the subhalo's most-bound particle before disruption. When orphans are included (and the effects of tidal stripping on stars are neglected), all simulations that adequately resolve the critical threshold yield a converged maximal satellite stellar mass function. Most orphans were accreted early, are found in the central regions of the main halo, and make up roughly half of all satellites in Aq-L1. Taking orphans into account there is no need to populate subhaloes below the critical threshold with satellites to fit the radial distribution of Milky Way satellites, as has been argued in recent work. Our model predicts that orphans dominate the ultrafaint population and that many more satellites with small apocentric radii should be detected in upcoming deep wide-field surveys.

Key words: galaxies: dwarf – galaxies: haloes - dark matter.

1 INTRODUCTION

The Λcold dark matter (ΛCDM) cosmological model describes a Universe where structure grows through gravitationally driven hierarchical clustering of dark matter clumps (see Frenk & White 2012, for a review). Galaxies form as gas cools and condenses at the centre of these dark matter 'haloes' (White & Rees 1978; White & Frenk 1991). The resulting distribution of dark matter structures, which resembles a cosmic web on large scales, has proved to be consistent with the observed large-scale distribution of galaxies at various epochs (e.g. Cole et al. 2005; Springel, Frenk & White 2006; Zehavi et al. 2011).

ΛCDM predicts a steep halo mass function across the entire mass range, from $\sim 10^{-6}\,M_\odot$ to $10^{15}\,M_\odot$ (Wang et al. 2012, for a 100 GeV dark matter particle). Furthermore, individual haloes are filled with 'substructure' consisting of the surviving inner regions of haloes that merged with the main halo progenitor at earlier times. These subhaloes also have a steep mass function, with thousands of low-mass systems expected within the virial radius of a host halo like that of our Milky Way (MW). In contrast, only ∼66 MW satellites have so far been identified, a discrepancy that gave rise to the long-standing misconception of a 'missing satellites' problem in ΛCDM (Klypin et al. 1999; Moore et al. 1999).

A simple solution to the 'missing satellites' problem envisions luminous subhaloes ('satellites', hereafter) forming only in haloes exceeding a 'threshold' or 'critical' mass, which means that satellites are only able to populate the few most massive subhaloes. The astrophysical processes that prevent galaxies from forming in haloes below the threshold mass were understood years before the 'missing satellites' was hailed as a problem for CDM.

Before the epoch of reionization, gas can condense and form stars only in haloes massive enough for atomic or molecular hydrogen to be able to cool (Tegmark et al. 1997; Benitez-Llambay & Frenk 2020). After reionization, the intergalactic medium is heated above 10^4 K and gas is only able to cool in haloes above a circular velocity approximately corresponding to the temperature of the ambient heated gas (Efstathiou 1992; Thoul & Weinberg 1996; Gnedin 2000; Benson et al. 2002a). These mechanisms impose a characteristic, redshift-dependent halo mass scale below which haloes remain dark (Benitez-Llambay & Frenk 2020).

Early work using semi-analytic models of galaxy formation applied to merger trees constructed from the extended Press–Schechter formalism showed how these mechanisms can be used to predict the abundance of satellites in the MW within the ΛCDM model (Kauffmann, White & Guiderdoni 1993; Bullock, Kravtsov &

★ E-mail: isabel.santos@durham.ac.uk

Weinberg 2000; Somerville 2002; Benson et al. 2002b). These papers predicted that MW-mass galaxies should have between 130 and 220 [90 per cent confidence level (CL)] satellites brighter than $M_V = 0$, although they were written when only the 11 'classical' satellites of the MW were known (Benson et al. 2002b).

In the past couple of decades, the census of satellites in the MW halo has expanded, with discoveries facilitated first by SDSS and, later, by deep imaging surveys such as DES, Pan-STARRS1, and HSC (e.g. Willman et al. 2005; Bechtol et al. 2015; Drlica-Wagner et al. 2015).Currently, 66 satellites are known to orbit the MW but, accounting for the selection function of these surveys and the recent accretion of the Large Magellanic Cloud (LMC), Newton et al. (2018) estimated that the MW should contain approximately 124^{+40}_{-27} (68 per cent CL) brighter than $M_V = 0$, in broad agreement with the early predictions of Benson et al. (2002b). Nadler et al. (2020) suggests an even larger estimate of 220 ± 50.

In the past few years, cosmological simulations of increasing sophistication and complexity have confirmed this result. Sawala et al. (2016) showed that the APOSTLE cosmological hydrodynamics simulations, based on the EAGLE code (Crain et al. 2015; Schaye et al. 2015), reproduce the stellar mass function of the classical satellites of the MW, for masses, $M_* > 10^5\,M_\odot$, in agreement with the earlier semi-analytic calculations.This result has also been echoed by other cosmological hydrodynamical simulations (e.g. Macciò et al. 2010; Simpson et al. 2018; Garrison-Kimmel et al. 2019). It is therefore puzzling that, in spite of this extensive body of theoretical work, references to the 'missing satellites' problem in ΛCDM are still found in the literature (eg. Homma et al. 2019).

Interestingly, the recent discovery of an increasing number of ultrafaint satellite galaxies in the MW halo has led to the opposite problem, namely that ΛCDM suffers instead from 'too many satellites'. This new perceived challenge to ΛCDM is predicated on the observation than there are more known satellites at small distances from the centre of the MW than there are surviving dark matter subhaloes at those distances massive enough to form a satellite in cosmological *N*-body simulations.

This apparent discrepancy led Graus et al. (2019) and Kelley et al. (2019) to argue that subhaloes of circular velocity as low as ∼7 km s^{-1} would need to harbour luminous satellites in order to reproduce the observed radial distribution of MW satellites. This velocity is much smaller than the ∼12 km s^{-1} corresponding to the critical threshold mass discussed above (Okamoto & Frenk 2009; Benitez-Llambay & Frenk 2020). A similar problem has been highlighted for other nearby galaxies by Carlsten et al. (2020).

However, it is important to point out that these studies did not fully take into account the extent to which the radial distribution of subhaloes orbiting a MW-like halo is affected by the artificial disruption of subhaloes that results from limited numerical resolution. Numerical convergence studies have shown that artificial disruption is important even for relatively massive subhaloes in the highest resolution *N*-body simulations available (see e.g. van den Bosch & Ogiya 2018; Errani & Navarro 2021). A proper comparison of the radial distribution of satellites in the MW and other galaxies with ΛCDM predictions therefore requires careful consideration of these artificially disrupted subhaloes.

In semi-analytic models of galaxy formation, satellites which have lost their dark matter subhaloes are often called 'orphans', and their existence has long been recognized as critical to explain the galaxy distribution in massive systems like galaxy clusters (e.g. Guo et al. 2011).

One of the main goals of this work is to assess the importance of orphan galaxies and how they affect the predicted abundance, radial distribution, and stellar mass function of satellite galaxies around MW-mass haloes. Our study makes use of the 'Aquarius A' halo of the Aquarius suite of *N*-body simulations (Springel et al. 2008). Aq-A is a MW-mass halo that was simulated at five different resolution levels, labelled L1 to L5; this allows a rigorous resolution study to be carried out. The Aq-A-L1 simulation (particle mass of $m_p = 1.7 \times 10^3\,M_\odot$) remains the highest resolution simulation of a MW halo ever carried out (see also Stadel et al. 2009, for a simulation of similar resolution). Our work is complementary to the statistical studies of this same halo by Han et al. (2016) and He, Han & Li (2024), who focus on disruption of dark subhaloes at lower masses than considered here.

To anticipate our main conclusions, we find that orphan galaxies are expected to be a major component of the satellite population, even in simulations with resolution as high as that of Aq-A-L1, where they make up roughly half of the total number of luminous satellites. Most orphan satellites are spatially concentrated, with many located tens of kiloparsecs from the host halo centre. Our study highlights the importance of properly modelling orphan satellites to ensure reliable predictions, especially as upcoming surveys (e.g. DESI, LSST, Roman, Euclid) will probe the ultrafaint regime with unprecedented depth.

Our results here represent the maximal satellite population in a MW-sized halo, rather than a direct prediction for comparison with observations, especially in the MW's inner regions. Indeed, some of these orphan satellites may suffer substantial stellar mass loss due to tides, or disrupt entirely, especially after the deepening of the potential well due to the assembly of the baryonic component of the host galaxy. We do not attempt to correct for these effects here, but intend to address them in a future contribution. Our goal here is instead to provide a prediction for the 'unabridged' population of all satellites in Aq-A; to check for convergence effects; and to assess which ΛCDM predictions regarding the full satellite population, including orphans, are most robust.

The paper is organized as follows. In Section 2, we introduce the simulations, models, and data used. In Section 2.3, we describe the treatment of orphan galaxies in GALFORM. In Section 3.1, we address dwarf galaxy formation in the GALFORM model and introduce the satellite sample that we will study. In Section 3.3, we present our results for the predicted luminosity function of satellites of MW-mass haloes while in Section 3.4, we present their radial distribution. In Section 3.7, we discuss the orbital evolution and present-day orbital properties of satellites galaxies. Finally, in Section 4 we summarize our conclusions.

2 METHODS

2.1 The Aquarius-A dark matter halo

We use a simulated halo from the Aquarius project (Springel et al. 2008), a suite of six dark matter-only MW-sized haloes simulated with the GADGET-3 code at five different resolution levels, L1 to L5. The Aquarius project adopts a flat ΛCDM cosmological model with parameters consistent with *Wilkinson Microwave Anisotropy Probe* (*WMAP*-5)[1] (Komatsu et al. 2009): $\Omega_m = 0.25$; $\Omega_\Lambda = 0.75$; $\Omega_{bar} = 0.045$; $H_0 = 100\,h$ km s^{-1} Mpc^{-1}; $\sigma_8 = 0.73$; $h = 0.73$.

[1]The use of more recent estimates of the cosmological parameters is not expected to introduce any relevant quantitative changes to our results.

Specifically, we study the so-called Aquarius-A halo (hereafter Aq-A), with virial[2] mass, $M_{200} = 1.8 \times 10^{12}$ $M_\odot$, virial radius, $r_{200} = 245.7$ kpc, concentration, $c_{NFW} = 16.11$, and virial velocity, $V_{200} = 179.4$ km s^{-1}, at $z = 0$.

In this work, we make use of resolution levels 1, 2, 4, and 5, corresponding to particle masses $m_p/M_\odot = [1.7 \times 10^3, 1.4 \times 10^4, 3.9 \times 10^5, 3.1 \times 10^6]$ and Plummer-equivalent gravitational softening lengths, $\epsilon/\mathrm{pc} = [20.5, 65.8, 342.5, 684.9]$, respectively. Aq-A-L1 remains to date the highest resolution simulation of a MW-mass halo, with ~ 4.4 billion particles in a $100\,h^{-1}$ Mpc cube and ~ 1.5 billion of them within the virial radius of the halo (see also Stadel et al. 2009). We refer the reader to table 1 of Springel et al. (2008) for more details on this particular halo.

At $z = 0$, the total halo mass and density profile of the Aq-A halo show excellent numerical convergence at all radii across resolution levels. A Navarro–Frenk–White profile (Navarro, Frenk & White 1996, 1997, hereafter NFW) provides an acceptable fit to the density profile, as shown by Navarro et al. (2010). Aq-A shows a steady growth in virial mass without major late-time mergers, reaching 10 per cent of its final total mass by cosmic time $t \sim 1$ Gyr, and 50 per cent by $t \sim 3.3$ Gyr. For reference, at $t = 0.5(1)$ Gyr, the virial radius of the main progenitor was $\sim 5(25)$ kpc (physical), the virial mass was $\sim 10^{9.7}(10^{11})$ $M_\odot$, and the virial velocity was $\sim 63(160)$ km s^{-1}.

Subhaloes in Aq-A were identified as self-bound substructures using the SUBFIND algorithm (Springel et al. 2001) applied to the friends-of-friends (FOF; Davis et al. 1985) group associated with the main halo. Embedded substructures survive within subhaloes, as expected from the hierarchical nature of structure formation in ΛCDM. A minimum of 20 particles are required to define and identify a subhalo at any time.

The substructure properties converge well between resolution levels (Springel et al. 2008). Specifically, at $z = 0$, the differential mass function of *surviving* subhalo converges well for masses $<5 \times 10^8$ $M_\odot$ (above this mass there are very few massive subhaloes, resulting in more scatter), down to the ∼20 particle limit. This mass function can be adequately approximated by a power law with slope −1.9 (see also Gao et al. 2004). Similarly, excellent convergence was also found in the cumulative subhalo maximum circular velocity (V_{max}) function, especially after correcting the velocities for the gravitational softening length in subhaloes with scale radii comparable to the gravitational softening (see equation 10 in Springel et al. 2008).

Springel et al. (2008) also studied the radial distribution of Aq-A-L1 subhaloes as a function of mass. They report that the number density profile of surviving subhaloes follows a 'universal' shape that is independent of subhalo mass and can be well described by an Einasto[3] profile with $\alpha = 0.678$ and $r_{-2} = 199$ kpc (see also Ludlow et al. 2009). This profile is substantially shallower than the dark matter profile in the inner regions, and implies that the majority of surviving subhaloes are found in the outskirts of the main halo. Even in our highest resolution simulation, no subhaloes are found at $z = 0$ within a distance of $r \sim 10$ kpc from the halo centre.

[2]Virial masses are measured within a sphere with mean density 200 times the critical value for closure. Virial quantities are identified with a '200' subscript.

[3]The Einasto profile may be written as $\ln \rho/\rho_{-2} = (-2/\alpha)[(r/r_{-2})^\alpha - 1]$.

2.2 The GALFORM semi-analytic model

We populate the dark matter haloes and subhaloes[4] of Aq-A with luminous galaxies using the Durham semi-analytical model for galaxy formation, GALFORM (White & Frenk 1991; Kauffmann et al. 1993; Cole et al. 1994, 2000; Lacey et al. 2016). GALFORM incorporates the many physical processes thought to govern the physics of galaxy formation and evolution, namely, the shock-heating and radiative cooling of gas in haloes, star formation in galaxy discs and in starbursts, feedback from supernovae and active galactic nuclei, chemical enrichment of stars and gas, and the photoionization of the intergalactic medium, among others.

The modelling of these processes relies on a set of parameters that have been constrained to reproduce various observational data sets. These include, at $z = 0$, the galaxy luminosity functions in different wavelengths, the H I mass function, and galaxy morphological fractions, as well as the number and redshift distribution of massive galaxies at high redshifts (we refer the reader to Lacey et al. 2016, for further details on the GALFORM model adopted here). GALFORM has also proven to be successful at reproducing many observables for which it was not tuned, such as the abundance of high redshift *JWST* galaxies (Cowley et al. 2018; Lu et al. 2024), or the main properties of the ultrafaint population of MW-like galaxies (e.g. Bose, Deason & Frenk 2018; Bose et al. 2020).

The most relevant aspects of the GALFORM model in relation to this study, which focuses on dwarf galaxies, are gas cooling, the impact of the ultraviolet (UV) background responsible for the reionization of the Universe and the impact of energy injected into the gas by supernovae. These effects are included in GALFORM in an approximate way, with gas cooling (and, hence, star formation) becoming ineffective in haloes whose virial masses are below the 'critical' mass, $M_{crit}(z)$, for galaxy formation proposed by Benitez-Llambay & Frenk (2020). Before reionization, $M_{crit}(z)$ is computed from the virial temperature required to collisionally excite neutral hydrogen. After reionization, the critical mass is set by the minimum gravitational potential able to overcome the pressure of photoheated gas, bringing it to the halo centre and igniting star formation. Calculation of M_{crit} before reionization was already included in early versions of GALFORM (Cole et al. 2000); after reionization, the 'v_{cut}' prescription in those early models has been replaced by an analytical fit to the Benitez-Llambay & Frenk (2020) calculation.

We refer the reader to Benitez-Llambay & Frenk (2020) for details on the critical mass calculation. For completeness, we list here the critical mass at various redshifts: at $z = 0$, 2, 10, 20; $M_{crit} = (5, 2, 0.08, 0.03) \times 10^9$ $M_\odot$, assuming a redshift of reionization, $z_{reion} = 6$ (Planck Collaboration VI 2020). At that time the critical mass has a mild jump, from $\sim 10^{8.1}$ $M_\odot$ to $10^{8.5}$ $M_\odot$. We discuss this further in Section 3.1.

Galaxy evolution in GALFORM varies if an object is a 'central' or a 'satellite' galaxy. In central galaxies (i.e. those forming in the main subhalo of a FoF halo), gas is allowed to cool and form stars at any time. On the other hand, as soon as a galaxy infalls into a more massive system and becomes a satellite (i.e. a subhalo of a central galaxy), GALFORM assumes instantaneous ram pressure stripping, meaning that all the diffuse gas of a subhalo is immediately stripped away and added to the hot gas reservoir of the host halo. Thereafter, gas is not allowed to accrete on to a satellite galaxy and thus no further cooling occurs. Only the pre-cooled gas in the satellite's cold gas reservoir can continue to fuel star formation after infall.

[4]In practice, GALFORM takes the simulation's merger trees and particle data as input.

GALFORM (in the version adopted here) does not account for tidal stripping of stars after a galaxy becomes a satellite. As a result, the stellar mass of a satellite remains effectively fixed at the value it had at infall (unless the galaxy retains some cold gas, which may slightly increase the stellar mass as that gas forms new stars).

Finally, GALFORM models galaxy mergers by computing, at each time-step, a merging time-scale for each galaxy with the central host galaxy. Specifically, a modification of the analytical Chandraskhar dynamical friction formula is used (see equation 6 in Simha & Cole 2017), which emulates the results of cosmological simulations of galaxy formation.

2.3 Orphan galaxies

It is now generally recognized that in cosmological *N*-body simulations many subhaloes, especially those of low mass, fully disrupt in the tidal field of the main halo. In early work, the tidal disruption of these objects was often interpreted as indicating that subhaloes genuinely disrupt (see e.g. Hayashi et al. 2003). Recent work, however, has shown that numerical limitations play a substantial role, artificially enhancing tidal disruption (den Bosch & Ogiya 2018). Indeed, for ΛCDM haloes, which typically have a cuspy NFW-like density profile, the central cusp is expected nearly always to survive the tides, even after intense and prolonged tidal stripping (Errani & Navarro 2021). Galaxies within artificially disrupted subhaloes in *N*-body cosmological simulations are often referred to in the literature as 'orphan' galaxies.

GALFORM follows orphans after their subhaloes fall below the 20-particle threshold and 'disrupt' by tracking the most bound particle of the subhalo at the last time-step when SUBFIND is able to identify it. The position and velocity of this particle is then assumed to be that of the orphan galaxy at later times. Orphans may survive to $z = 0$ or may be deemed to merge with the central galaxy at a time determined by the Chandrasekhar dynamical friction time-scale computed just before the subhalo disrupts.

GALFORM thus classifies galaxies into three types: 'type-0': galaxies in resolved subhaloes that are centrals in their FOF group; 'type-1': galaxies in 'surviving', or resolved subhaloes; and 'type-2' or 'orphans': satellite galaxies in disrupted or unresolved subhaloes. We shall make use of this nomenclature throughout this paper.

2.4 Orbital evolution of surviving and orphan satellites

Fig. 1 illustrates the orbital evolution of examples of satellite galaxies of type-1 (surviving subhalo, left panels) and type-2 (disrupted subhalo, right panels), chosen to highlight the main characteristics of each type. The various panels show the time evolution of the radial distance from the centre of the host halo (top), of the subhalo maximum circular velocity, $V_{\rm max}$ (middle), and of the number of bound particles (or the equivalent subhalo bound mass, $M_{\rm bound}$, see twin axis; bottom). The temporal evolution of the virial radius of the main halo is depicted in the upper panels with a solid red line.

Black lines indicate times when the subhalo is resolved as a surviving self-bound system. Times marked with a black circle indicate that the galaxy is type-0 (i.e. central in its own FoF halo). In the case of the type-2 galaxy, the background of the figure is shaded grey once the subhalo becomes unresolved and the galaxy transitions into the 'orphan' state. From that moment onward, the satellite is tracked by the most bound particle of its subhalo at the last time-step it was resolved, and is shown by the solid blue line.

Vertical lines mark different characteristic times in the evolution of a satellite. The red dotted line indicates the time of infall into the host halo, $t_{\rm acc}$, defined as the time when the galaxy's radial distance first crosses the host halo's evolving virial radius. The black dotted vertical lines indicate the time, before infall, when the number of particles associated with the subhalo reaches its maximum, which we denote as $t_{\rm peak}$. The corresponding values of $V_{\rm peak}$ and $M_{\rm peak}$ of these examples are listed in the bottom panel legend.

In the two examples, $t_{\rm peak}$ occurs quite early ($\lesssim 3$ Gyr). For reference, in the implementation of GALFORM adopted here, the time of reionization is only slightly earlier, $t_{\rm reion} \sim 0.95$ Gyr ($z_{\rm reion} = 6$). For the type-1 satellite, $V_{\rm peak}$ is 26 km s^{-1}, while for the type-2 it is 18 km s^{-1}. As for the bound mass, the type-1 and type-2 satellites reach, at $t_{\rm peak}$, a maximum of $1.4 \times 10^9\,{\rm M}_\odot$ and $1.4 \times 10^8\,{\rm M}_\odot$, respectively.

These satellites add a relatively small amount of mass to the main halo, which, at $t = 2$ Gyr, already had a virial mass of $5 \times 10^{11}\,{\rm M}_\odot$ and a virial radius of ∼50 kpc. The stellar mass assigned by GALFORM to each of these systems is shown by the green curves in the bottom panel. These show that star formation in GALFORM satellites typically ends shortly after infall into the main halo; the stellar mass thus remains roughly constant thereafter, without correction for possible tidal mass losses.[5]

After infall, both satellites quickly settle on to fairly stable orbits of constant apocentric and pericentric distances and relatively short orbital times. This is because although the main halo keeps accreting mass, little of that mass reaches the inner regions; indeed, the total mass enclosed within 50 kpc of the main halo remains essentially constant after $t = 3$ Gyr.

Note that the final apocentric distance is strongly correlated with the virial radius of the main halo at the time of infall. For the type-1 example, the final apocentric distance is ∼80 kpc, whereas the virial radius at $t_{\rm acc} = 3$ Gyr was 87 kpc. The corresponding numbers are ∼43 kpc and 43.5 kpc for the type-2 example, which was accreted at $t_{\rm acc} = 1.5$ Gyr. We shall see below that these broad correlations are followed by all satellite systems identified and tracked by GALFORM.

The evolution of both satellites shows clear signs of heavy tidal stripping after accretion. The bound mass of the type-1 satellite decreases by more than 2 orders of magnitude after being accreted into the main halo. The type-2 satellite loses at least as much, and becomes unresolved after reaching a few hundred particles, when SUBFIND loses track of it.

2.5 Aq-A satellites

We focus on the satellite galaxies of the Aq-A host galaxy at $z = 0$, identified by GALFORM in four different realizations of the halo at different resolutions. To recall, we define as satellites all subhaloes to which GALFORM has assigned a luminous component (i.e. stars) and located within 300 kpc from the centre of the main host galaxy halo.[6] This limiting radius is slightly larger than the Aq-A virial radius, $r_{200} = 245$ kpc at $z = 0$. We adopt 300 kpc to facilitate comparison with earlier work, which have conventionally adopted 300 kpc as a fiducial 'virial radius' for the MW and M31 haloes.

[5]We use the tidal stripping framework of Errani et al. (2022) to estimate tidal mass losses in a forthcoming paper.

[6]This definition implies that not only galaxies classified as type-1 and 2 in GALFORM are considered satellites, but also any type-0 within 300 kpc from the main halo centre. We note that their contribution is, however, negligible: we find fewer than 2 type-0s within 300 kpc. These have been added to the type-1 population.

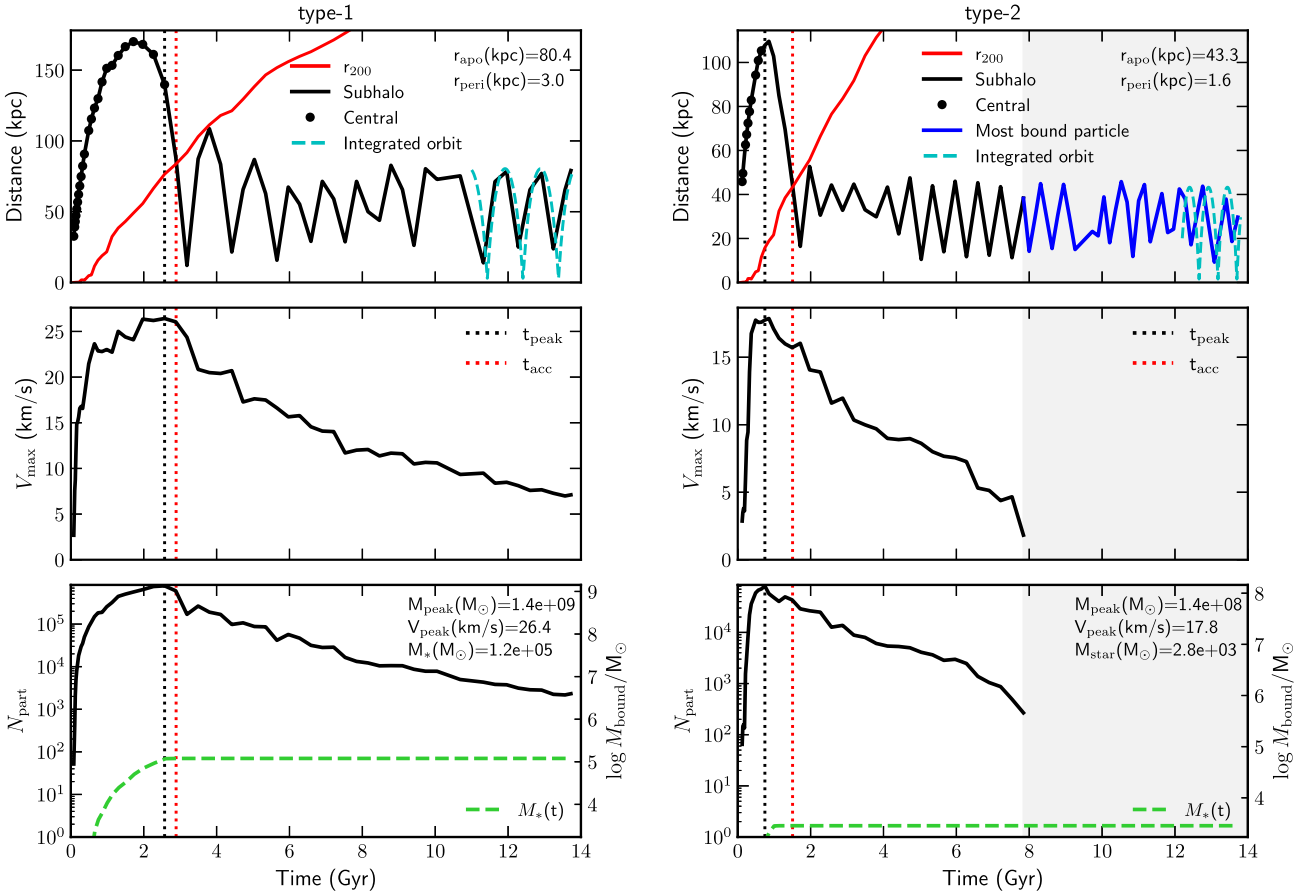

Figure 1. Evolution of example type-1 (left) and type-2 (right) satellites in Aq-A-L1. The panels show the radial distance of the galaxy from the centre of the Aq-A halo (top), the maximum circular velocity V_{max} (middle), and the bound number of particles (and equivalent subhalo bound mass, M_{bound}, see right y-axis in the bottom panels), as a function of the age of the Universe. The bottom panels also include, in green, the stellar mass of the subhalo, which remains essentially constant after accretion into the main halo as star formation ceases after accretion and stellar tidal mass loss is not considered in this work. Solid black lines show satellite data from the SUBFIND catalogue (while the subhalo is resolved). Black circles indicate when the galaxy is classified as the central of its FoF group. In the case of the type-2 galaxy, the background is shaded grey after the galaxy becomes an orphan and starts to be tracked via its most bound particle (shown with a solid blue line). The red solid line shows the time evolution of the virial radius, r_{200}, of the Aq-A-L1 halo. Vertical dotted lines indicate different characteristic times in the evolution of the satellite: the time when the circular velocity peaks (t_{peak}, in grey) and the time of first infall into the main halo (t_{acc}, in red); see the text for their definitions. The dashed cyan lines indicate the orbits integrated backwards in the gravitational potential of Aq-A-L1 from the $z = 0$ position and velocity.

Using merger trees we are able to track all satellites back in time, and measure their properties as a function of time. We shall focus on M_*, the satellite stellar mass at $z = 0$; its infall time, t_{acc}, defined as the first time it enters the evolving virial radius of the main progenitor; and on the orbital parameters at $z = 0$, such as pericentric and apocentric radii (r_{peri} and r_{apo}). We note that a few satellites show recent infall times today, which could lead to future apocentres exceeding $r_{200}(t)$ (i.e. 'backsplash' galaxies). Careful inspection of the orbital histories of all satellites however confirms that all luminous objects found within 300 kpc are indeed bound to the host halo, and no escaping galaxies are included in our satellite sample.

We also track the satellite 'peak' circular velocity (V_{peak}), defined as the maximum circular velocity, V_{max}, at the time, before infall, when the SUBFIND mass of a subhalo is maximal. We also identify the time when a galaxy formed its first stars, t_{fstr}, according to GALFORM. In GALFORM, gas can only begin forming stars in galaxies that are centrals, so t_{fstr} in general precedes t_{acc}.

Special care has been taken to weed the GALFORM satellite list of spurious objects, such as low-mass objects where stars have been allowed to form only because the identity of the halo has been temporarily swapped with that of a more massive neighbour, as well as various other merger-tree artefacts in the low-mass regime. We use this cleansed galaxy list to present, in the following section, our results for the abundance, radial distribution, and orbital evolution of the full, unabridged luminous satellite population of the Aq-A halo, with special emphasis on the contribution of orphan satellites.

2.6 Milky Way satellites

We shall compare our results to the observational data of known MW satellite galaxies. This comparison is necessarily qualitative at this stage, both because the census of MW satellites remains highly incomplete, and because our results need to be modified to include stellar tidal stripping in both type-1 and type-2 satellites. As for Aq-A, we shall consider as MW satellites all known dwarfs found within 300 kpc of the MW centre, which results in a sample of 66 satellites; see Appendix A for details. While this limiting radius corresponds to the virial radius of a halo of total mass larger than current estimates for the MW ($M_{200}^{MW} \simeq 10^{12}$ M$_\odot$, which corresponds to $r_{200} = 207$

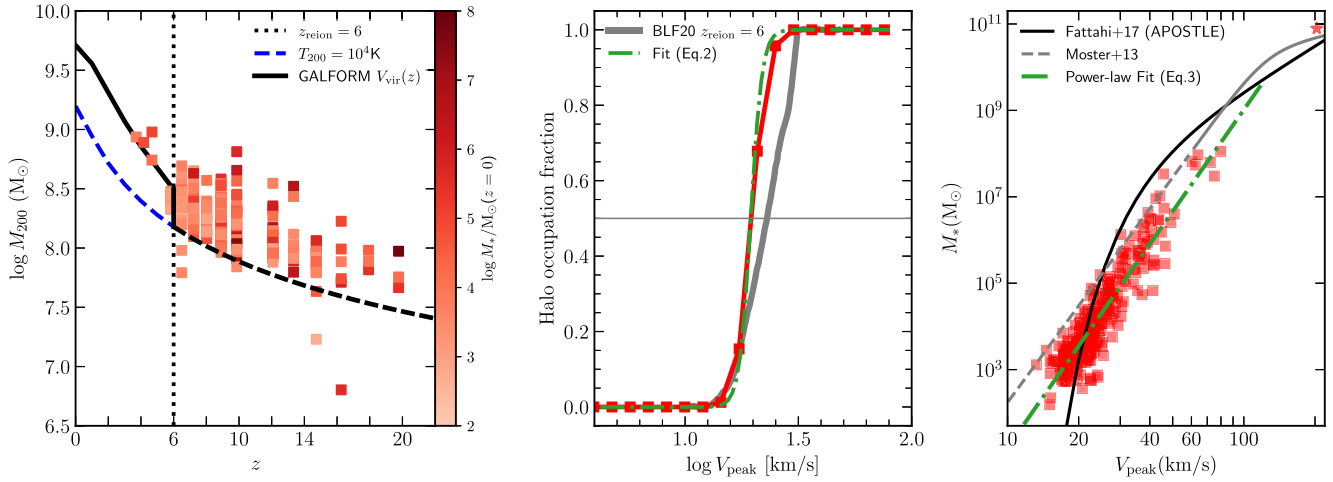

Figure 2. Galaxy formation in Aq-A-L1 according to GALFORM. *Left:* redshift of formation of the first stars in a halo ($t_{\rm fstr}$) as a function of halo mass, M_{200}, at that time. The redshift of reionization, $z_{\rm reion} = 6$, is marked by a vertical line. Thick black lines illustrate the evolution of the critical mass, $M_{\rm crit}$ introduced by Benitez-Llambay & Frenk (2020). Before reionization (dashed linetype), $M_{\rm crit}$ roughly tracks the 'hydrogen cooling limit', i.e. the mass of a halo of virial temperature $T_{200} = 10^4$ K. After reionization (solid linestyle), $M_{\rm crit}$ equals the halo mass above which photoheated gas cannot remain in hydrostatic equilibrium and thus collapses. *Middle:* halo occupation fraction (HOF) of haloes in Aq-A-L1. The HOF from Benitez-Llambay & Frenk (2020), assuming $z_{\rm reion} = 6$, is plotted in grey for comparison. A green dot–dashed line shows our analytical fit to the HOF (equation 2). *Right:* the GALFORM M_*–$V_{\rm peak}$ relation for Aq-A satellites. For comparison, the black curve shows the relation obtained in the APOSTLE simulations (Fattahi et al. 2018) and the grey line shows the abundance-matching relation of Moster, Naab & White (2013) extrapolated (in dashed linetype) to lower masses. A star symbol shows the data point corresponding to the central host galaxy. The green dot–dashed line shows the best power-law fit to the data points, with parameters given in equation (3).

kpc; see Cautun et al. 2020), it is the radius commonly used to define the satellite populations of the MW and M31 in the literature. Had we only used satellites within $r_{200} = 207$ kpc the list would have not included Indus2, Bootes4, CanesVenatici1, Leo1, Leo2, Cetus3, and Eridanus2, and would be reduced to 59 MW satellites.

We use positions (RA, Dec.) and distances ($m - M$) data from the latest update of the McConnachie (2012) Nearby Dwarf Galaxy Database[7], and compute Galactocentric positions and velocities assuming a Galactocentric distance for the Sun of $R_\odot = 8.29$ kpc, a circular velocity for the local standard of rest (LSR) of $V_0 = 239$ km s^{-1} (McMillan 2011), and a peculiar velocity with respect to the LSR of $(U_\odot, V_\odot, W_\odot) = (11.1, 12.24, 7.25)$ km s^{-1} (Schönrich, Binney & Dehnen 2010).

In Section 3.7, we shall compare our results to data for the subset of MW satellites with available 3D kinematical information (47 objects). We compute pericentric and apocentric distances using the Cautun et al. (2020) MW potential, which assumes a virial mass for the MW of $M_{200} = 1.08^{+0.20}_{-0.14}\,M_\odot$ consistent with recent estimates (e.g. Callingham et al. 2019). Since this potential is truncated at 300 kpc we extrapolate the mass distribution beyond this radius assuming an NFW mass profile with the same M_{200}, when needed. The Cautun et al. (2020) potential is static and includes different MW baryonic components (i.e. bulge, thin, and thick stellar disc, H I disc, molecular gas disc, and diffuse gas halo), following parameters that best fit the latest *Gaia* rotation curve data (Eilers et al. 2019). It also includes the effects of dark matter halo contraction from baryon effects. We estimate orbital parameters by integrating the $z = 0$ position and velocity data of MW satellites back in time for ∼1 Gyr. The integration neglects the effects of dynamical friction and time evolution in the host potential, which are likely negligible given the short integration time and the relatively small satellite halo masses. The potential effects of a massive companion like the LMC are also not considered here (see instead Patel et al. 2020; Battaglia et al. 2022).[8] The derived pericentric and apocentric distances are listed in Table A1.

3 RESULTS

3.1 Satellite galaxies in GALFORM

We begin our discussion by showing explicitly which haloes are able to harbour luminous galaxies in the implementation of GALFORM chosen in this work. As discussed in Section 2.2, before reionization, stars can form only in haloes massive enough for hydrogen cooling to take place and, after reionization, in haloes massive enough for gravitationally collapsing cooling gas to overcome the pressure induced by photoheating. There is therefore a redshift-dependent critical halo mass at all times, $M_{\rm crit}(z)$, above which stars can form, as described in detail by Benitez-Llambay & Frenk (2020). We show this limiting mass as a function of redshift as the thick black curves in the left-hand panel of Fig. 2. Dashed linetype corresponds to redshifts before reionization, $z_{\rm reion}$; solid after $z_{\rm reion}$.

For comparison, a blue curve indicates the mass of haloes with constant virial temperature, $T_{200}/{\rm K} = (\mu m_p/2k_B)(V_{200}/{\rm km\ s^{-1}})^2 = 10^4$ K after reionization. The conversion from velocity to degrees K assume a mean molecular weight of $\mu = 0.597$ before and after reionization.

[7]See https://www.cadc-ccda.hia-iha.nrc-cnrc.gc.ca/en/community/nearby/ and references therein.

[8]We have compared our results using the Cautun et al. (2020) MW model with those of Li et al. (2021) and Battaglia et al. (2022) (who assume a lighter MW halo and the presence of the LMC in the case of the latter). While differences in the assumed MW halo mass and the inclusion or exclusion of the LMC naturally affect the precise values of the inferred MW satellite orbital parameters, all models broadly agree on the overall parameter space occupied by satellites on the $r_{\rm peri} - r_{\rm apo}$ plane, which is what we shall focus on in this study.

The square symbols show results for all Aq-A $z = 0$ satellites at the time, $t_{\rm fstr}$, of their first star formation episode (i.e. at the time when they first appear in the GALFORM galaxy catalogue). We only include in the plot systems which were centrals (i.e. type-0s) at that time, to ensure that their virial mass estimates, $M_{200}(t_{\rm fstr})$, are reliable. (Indeed, if a subhalo has already become a satellite of the Aq-A host halo, its mass is ill-defined due to tidal effects.) Squares in Fig. 2 are coloured according to the stellar mass of the system at $z = 0$. This figure shows that, as expected, luminous satellites mostly form in haloes which, at some time in their formation history, have had virial masses exceeding the critical line. Note as well that the great majority of satellites started forming stars before reionization; only a handful form their first stars after $z_{\rm reion} = 6$.

Most luminous systems start forming stars barely ∼0.3 Gyr after the big bang. The last Aq-A-L1 satellite to begin forming stars does so at $t_{\rm fstr} = 7.5$ Gyr, i.e. 6 Gyr ago. As noted by Benitez-Llambay & Frenk (2020) and Pereira-Wilson et al. (2023), this explains why all MW satellites, regardless of mass, have at least some fraction of their stars in a very old stellar population. In simple terms, most haloes able to form stars become eligible to do so very early on. Note that, at the time of the formation of their first star, most subhaloes had virial mass exceeding $10^{7.5}$ M$_\odot$. This is not a result of limited numerical resolution but of the physics of cooling gas. Indeed, such haloes are well resolved in Aq-A-L1, with at least $10^{4.2}$ particles.

The existence of a critical mass imposes a strong mass limit on the Aq-A satellite population, which is best appreciated by considering the 'occupation fraction' as a function of $V_{\rm peak}$, i.e. the fraction of Aq-A subhaloes (identified at $z = 0$) which harbour luminous satellites, shown in the middle panel of Fig. 2. Note the sharp transition from completely 'dark' subhaloes to luminous ones: all subhaloes with $V_{\rm peak} < 13$ km s^{-1} are dark, and all subhaloes with $V_{\rm peak} > 28$ km s^{-1} have stars. These results are in line with earlier work, particularly that by Okamoto & Frenk (2009) who adopted a minimum halo circular velocity of 12 km s^{-1} for hydrogen to begin cooling and forming stars. They are also very close to the analytic results of the Benitez-Llambay & Frenk (2020) model (depicted by the grey line). For that model, the occupation fraction is 50 per cent at $V_{\rm peak} = 23$ km s^{-1}. In Aq-A-L1, the 50 per cent halo occupation is reached at $V_{\rm peak} = 19.5$ km s^{-1}.

GALFORM also predicts a strong dependence of the galaxy stellar mass of a satellite on $V_{\rm peak}$, as shown in the right-hand panel of Fig. 2. Note the tight dependence of the galaxy stellar mass on this measure of the depth of the subhalo potential well. We note that $V_{\rm peak}$ may differ significantly from $V_{\rm max}$ (the maximum subhalo circular velocity at $z = 0$) as the latter could have been strongly affected by tides. We also note that M_* in Fig. 2 refers to the stellar mass returned by GALFORM, which does *not* include any loss of stars due to tidal stripping. Tidal effects on the stellar component are likely to be important for some satellites, especially those that evolve to become an orphan at $z = 0$. We intend to address this important issue in detail in a future contribution.

The GALFORM satellite luminosity (or stellar mass) function will depend strongly on the M_*–$V_{\rm peak}$ relation shown in the right-hand panel of Fig. 2 so it is instructive to compare it to the results of the cosmological hydrodynamical simulations from the APOSTLE project (solid line; Fattahi et al. 2018), and of the abundance-matching model of Moster et al. (2013). The differences between models highlights our uncertain understanding of how dwarf galaxies populate low-mass haloes. Indeed, each of these models would yield significantly different satellite luminosity functions for the same $V_{\rm peak}$ function, which is the true robust prediction of ΛCDM. Although we will present results for the Aq-A satellite luminosity function below, one should bear in mind this model dependency before drawing strong conclusions.

In summary, the implementation of GALFORM adopted here allows luminous satellites to form efficiently only in subhaloes which exceed at some point a threshold peak circular velocity of ∼ 15 km s^{-1}. The peak circular velocity of a subhalo (typically reached just before first infall into the main halo) determines, with little scatter, the satellite stellar mass at the time of infall. Any modification to this model would inevitably have a quantitative impact on our results regarding the abundance of satellite galaxies, which we explore next.

3.2 The Aq-A subhalo peak-velocity function

As discussed in the previous section, the $V_{\rm peak}$ function of *all* accreted subhaloes in the Aq-A-L1 simulation (which did not merge with the main halo) underpins the GALFORM model predictions for the satellite luminosity function. In this section, we study the $V_{\rm peak}$ function of Aq-A-L1 subhaloes and satellite galaxies, and introduce a simple model to estimate the GALFORM satellite luminosity function of ΛCDM host haloes of arbitrary mass.

Wang et al. (2012) showed that the $z = 0$ abundance of subhaloes within r_{200} of a host halo, when plotted as a function of $\nu = V_{\rm max}/V_{200}$, is independent of host halo mass (see their fig. 3). The cumulative subhalo $V_{\rm max}$ distribution may be approximated by a simple power law: $\langle N_{\rm sub}\rangle(>\nu) = 10.2(\nu/0.15)^{-3.11}$ in the range $0.1 < \nu < 0.5$. Thus, the total number of subhaloes, expressed as a function of $\nu_{\rm p} = V_{\rm peak}/V_{200}$, is also expected to be roughly independent of host halo mass.

In order to make it relatively straightforward to scale our results for Aq-A to other choices of the virial mass/radius/velocity of the main halo, we shall limit the discussion in this section to subhaloes that end up, at $z = 0$, within the virial radius of the main halo $r_{200} = 245$ kpc. Note that this choice of limiting radius is different from the 300 kpc used in the rest of the paper and chosen to compare with the MW satellite population.

We begin the discussion by comparing, in Fig. 3, the differential $V_{\rm max}$ function for surviving subhaloes in Aq-A-L1 (dashed grey line) with the fitting formula proposed by Wang et al. (2012) (thick dashed black line), and find them in good agreement. Note that $V_{\rm max}$ refers to the maximum circular velocity of subhaloes at $z = 0$, and not to $V_{\rm peak}$.

The $V_{\rm peak}$ function of surviving subhaloes is shifted to higher velocities relative to the $V_{\rm max}$ function, as shown by the thick solid grey line in Fig. 3. The velocity shift, of order ∼60 per cent, is nearly constant for all subhaloes. The largest subhaloes in Aq-A have $\nu_{\rm p} \sim 0.4$–0.5, which corresponds to ∼70–80 km s^{-1}. This limit is only a factor of ∼5 larger than the minimum value of $V_{\rm peak}$ ∼15 km/s^{-1} needed for a subhalo to be able to harbour a luminous galaxy. Therefore, the whole satellite luminosity function reflects the abundance of subhaloes over a very narrow range of $V_{\rm peak}$, from ∼15 to ∼80 km s^{-1}.

This is shown by the thick solid red line in Fig. 3, which corresponds to the $V_{\rm peak}$ distribution of type-1 satellites. As expected, this tracks the solid grey line closely down to $\nu_{\rm p} \sim 0.1$ (i.e. $V_{\rm peak} \sim 20$ km s^{-1}) where it becomes exponentially truncated by the plummeting occupation fraction at low $V_{\rm peak}$ (see middle panel of Fig. 2). No type-1 satellites are found with $\nu_{\rm p} < (15/179) = 0.08$.

Adding the 'orphan' satellite population yields the thick blue curve, which leads to an increase in satellite numbers, especially at $\nu_{\rm p} \sim 0.1$, near the truncation value. No orphans are found, either, below $\nu_{\rm p} = 0.08$.

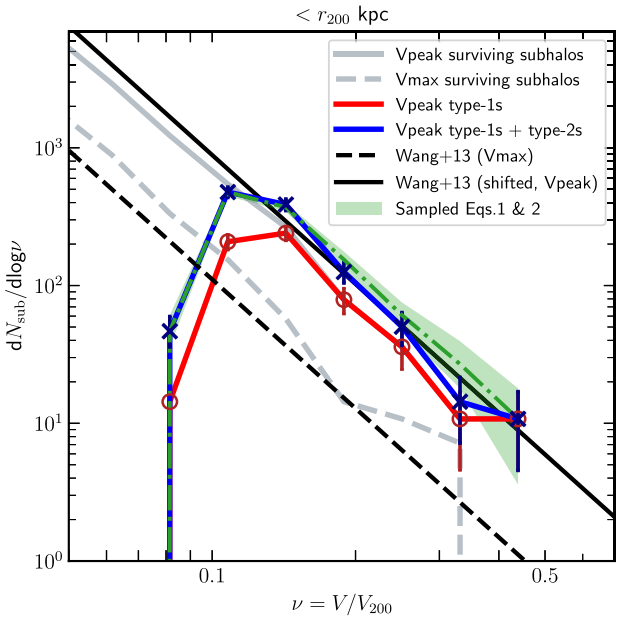

Figure 3. Differential number of galaxies (or subhaloes) as a function of ν, defined as the velocity in units of the main halo virial velocity (i.e. either V_{max}/V_{200} in dashed linetype or $V_{\mathrm{peak}}/V_{200}$ in solid linetype; see legend). Light grey lines show the differential subhalo V_{max} (dashed) and V_{peak} (solid) scaled functions for surviving subhaloes in the dark matter-only Aq-A-L1 simulation. A black dashed line shows the scaled subhalo V_{max} function from Wang et al. (2012). Red and blue solid lines indicate the relations obtained for galaxy samples: type-1s only, and the total sample of satellites (type-1s + type-2s), respectively. The solid black line is the Wang et al. (2012) relation, shifted by 0.29 dex in log ν to match the blue curve at large values of ν (see equation 1). The green shaded region shows the result of Monte Carlo sampling the subhalo V_{peak} function (equation 1) and filtering it by the HOF (equation 2). See the text for details.

We may approximate the total satellite ν function by sampling the V_{peak} relation (black solid line) obtained by shifting the Wang et al. (2012) function in velocity to match the blue curve. In differential form, this function may be written as

$$\mathrm{d}N/\mathrm{d}\log\nu = a(\nu/\nu_0)^b, \tag{1}$$

with $a = 660$, $b = -3.11$, and $\nu_0 = 0.11$. This function is then filtered according to the HOF from this GALFORM model (see middle panel in Fig. 2). An analytical fit to the HOF (shown with a green dashed line in that panel) is given by

$$\mathrm{HOF} = (1 + \tanh((x - x_0)/x_1))/2, \tag{2}$$

where $x = \log V_{\mathrm{peak}}/\mathrm{km\ s^{-1}}$, $x_0 = 1.29$, and $x_1 = 0.05$. The green line and shaded region in Fig. 3 show the resultant mean and $\pm 1\sigma$ uncertainty from 100 random realizations.

These functions, together with a prescription relating V_{peak} to M_*, are enough to characterize the full, unabridged satellite population of a MW-sized halo. The GALFORM V_{peak}–M_* relation is well approximated by a power law,

$$M_* = 9 \times 10^8\,(V_{\mathrm{peak}}/100\,\mathrm{km\,s^{-1}})^{7.8}\,\mathrm{M}_\odot, \tag{3}$$

shown by a green dashed line in the right-hand panel of Fig. 2, with ∼0.4 dex scatter in mass. Using the above expressions, we can analytically estimate the differential abundance of satellites as a function of mass (see green shaded area in the bottom panel of Fig. 4).

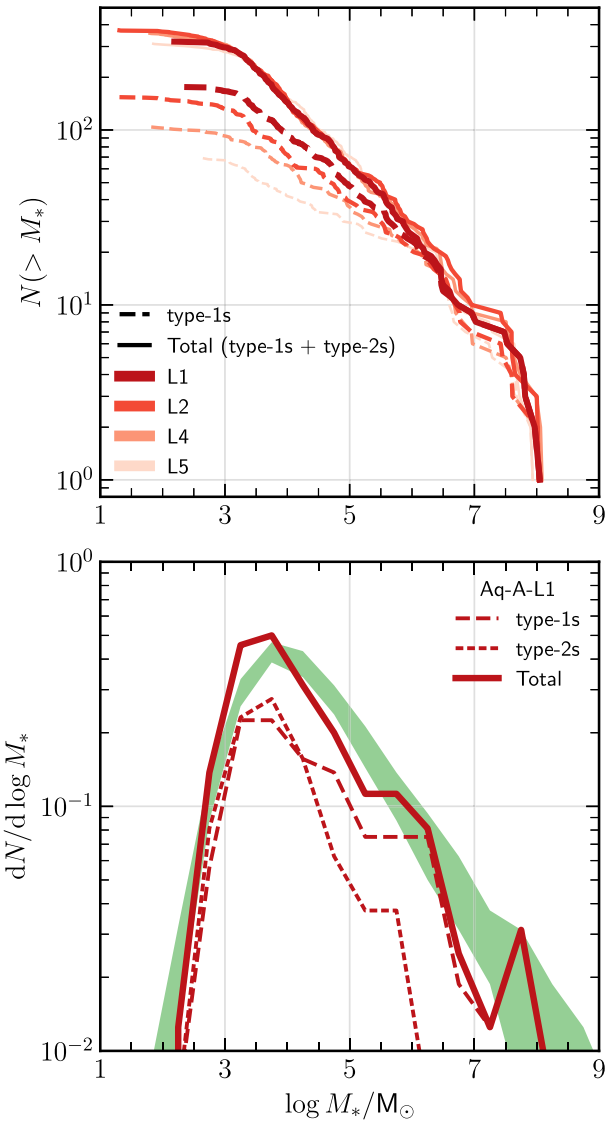

Figure 4. *Top:* satellite stellar mass function of Aq-A. Lines of different colour/thickness correspond to GALFORM results for runs at different resolution levels. Dashed lines indicate the functions obtained when counting only type-1 satellites (i.e. satellites in surviving subhaloes). The solid lines show the total results, including both type-1s and type-2s. *Bottom:* differential satellite luminosity function for Aq-A-L1, our highest resolution run. We show separately the contribution from type-1s, type-2s, and the total. The green shaded area shows the result of using the 'filtered' satellite subhalo V_{peak} function (see Fig. 3) together with the M_*–V_{peak} relation to predict the satellite mass function.

3.3 The Aq-A satellite stellar mass function

As discussed above, the satellite stellar mass function follows from the peak velocity function explored in the previous section, together with the tight V_{peak}–M_* relation shown in the right-hand panel of Fig. 2. We show the Aq-A satellite stellar mass function within 300 kpc at $z = 0$ predicted by GALFORM for the various resolution levels in Fig. 4. The top panel shows the cumulative function, whereas the bottom panel shows the same data in differential form, but only for the highest resolution run, Aq-A-L1.

The solid lines in the top panels of Fig. 4 show results for *all* satellites; i.e. surviving (type-1s) plus orphan (type-2s) systems. Different colours indicate different resolution levels; the thickness of

the curves increases as the resolution improves. The contribution of type-1s (surviving) satellites is shown by the dashed lines of matching colour. We recall that tidal stripping of stars is not modelled in the implementation of GALFORM used for this study, so these mass functions are best thought as corresponding to the 'infall' or 'peak' stellar mass function of Aq-A satellites.

Note the excellent convergence for the different resolution levels when *all* satellites are considered (all solid lines are basically on top of each other), although it is clear that the contribution of orphan systems becomes more and more important as the resolution becomes poorer. Type-1s are more prevalent at higher resolution, with no sign of convergence, even in the highest resolution runs. This is a clear indication that, even at the very high resolution of L1, orphan satellites need to be considered to account for the full satellite population of a MW-sized halo. When orphans are included, all simulations converge. This is a reflection of the relatively high halo mass 'threshold' needed to host a luminous system; indeed, haloes of $V_{\rm peak} > 15$ km s^{-1} (corresponding to a virial mass of $\sim 10^9\,{\rm M}_\odot$ at $z = 0$) are well resolved at all resolution levels of the Aq-A halo.

GALFORM predicts roughly ∼300 Aq-A satellites with 'peak' stellar masses above $10^3\,{\rm M}_\odot$, and fewer than ∼400 luminous satellites of all luminosities. For our highest resolution run, *half of those satellites are orphans*, a fraction that increases gradually at lower resolution. We note that these numbers cannot be readily compared with extant data for the MW satellite population, because they are particularly sensitive to the virial mass of the halo, to the redshift dependence of the mass threshold for galaxy formation, $M_{\rm crit}$, in the model, as well as to possible corrections for tidal stripping, which have not been considered here. Increasing or decreasing the halo virial mass will affect almost linearly the predicted satellite numbers. Varying the reionization redshift also has an effect, because it leads to a change in $M_{\rm crit}(z)$, as we show in Appendix B.

Although the total number of satellites is sensitive to modelling details, one robust prediction is the presence of a well-defined peak in the differential satellite stellar mass function, at the stellar mass corresponding to that of a galaxy that forms in a subhalo with $V_{\rm peak} \sim 20$ km s^{-1}, below which the 'halo occupation fraction' drops dramatically (see middle panel in Fig. 2). In the GALFORM implementation we adopt here, the peak is at $\sim 10^{3.5}\,{\rm M}_\odot$ (right-hand panel of Fig. 2), reflecting the fact that below $V_{\rm peak} = 20$ km s^{-1}, more and more subhaloes remain 'dark', and those that become satellites reach stellar masses $M_* > 10^{3.5}\,{\rm M}_\odot$.

The peak at $10^{3.5}\,{\rm M}_\odot$ does not seem to be a result of resolution, since it is seen at all resolutions. Importantly, it is seen in both type-1 and type-2 satellite mass functions. It may therefore be considered a robust prediction of models that combine a tight $V_{\rm peak}$–M_* relation with a smoothly evolving $M_{\rm crit}(z)$. The actual location of the peak depends sensitively on the M_*–$V_{\rm peak}$ relation. However, for the current GALFORM implementation, it does not change when varying $z_{\rm reion}$, as we discuss in the Appendix B. Identifying a well-defined peak in the stellar mass function of MW satellites would help to put strong constraints on the validity of this type of modelling.

Our conclusion is qualitatively similar to that of Bose et al. (2018), who argued that cosmic reionization gives rise to a bimodal satellite stellar mass function. A bimodal distribution can be seen in the bottom panel of Fig. 4. The two peaks, at $M_* \simeq 10^{3.5}\,{\rm M}_\odot$ and $M_* \simeq 10^6\,{\rm M}_\odot$, are in the same location as in Bose et al. (2018) but the second peak is less prominent in our study. The stronger bimodality in Bose et al. (2018) reflects the sharp threshold, $V_{\rm peak} > 30$ km s^{-1}, for star formation after $z_{\rm reion}$ which alters the M_*–$V_{\rm peak}$ relation. The gentler evolution of $M_{\rm crit}(z)$ across reionization that results from the Benitez-Llambay & Frenk (2020) model implemented here reduces the prominence of the bimodality.

Finally, in the bottom panel of Fig. 4, we present, as a green shaded region, the satellite mass function predicted following the analytical model introduced in Section 3.2. This is obtained by combining the HOF-filtered satellite subhalo $V_{\rm peak}$ function with the $M_* - V_{\rm peak}$ relation (see equations 1, 2, and 3). Specifically, the green area covers the $\pm 1\sigma$ dispersion from 100 random realizations of this model. As expected, the resulting analytical estimate closely reproduces the satellite distribution of the Aq-A-L1 simulation.

3.4 The spatial distribution of Aq-A satellites

Fig. 5 shows a randomly oriented projection of the Aq-A-L1 halo and its satellite population at $z = 0$. The background is an image of the halo where the brightness of each pixel is given by the projected dark matter density and the colour intensity is determined by the local velocity dispersion of dark matter particles. This rendition emphasizes visually the presence of the smallest haloes.

The positions of satellite galaxies are overplotted: surviving (type-1) systems as open red circles, orphans (type-2s) as magenta crosses. Type-1 satellites lie on top of small subhaloes, as expected, whereas type-2s lack a corresponding dark matter counterpart. Aq-A-L1 resolves a large number of subhaloes, much larger than the total number of luminous satellites predicted by GALFORM. For reference, in Aq-A-L1 there are 190 453 resolved subhaloes within 300 kpc at $z = 0$, all with bound masses $> 3 \times 10^4\,{\rm M}_\odot$ (i.e. > 20 particles). About ∼4000 of these have, at present, $V_{\rm max} > 5$ km s^{-1}. As discussed in the previous sections, only 176 of these surviving subhaloes host luminous satellites (circles in Fig. 5). A similar number of satellites (144) are orphans (crosses).

The right-hand panel of Fig. 5 shows a zoomed-in view of the central 50 kpc region. (The zoomed region is a slice that excludes systems with $|z| > 50$ kpc to minimize the inclusion of distant satellites projected along the line of sight.) As expected, most type-2s are located close to the centre of the halo, whereas type-1s are found in general at larger radii.

As may be seen in Fig. 5, luminous satellites are more centrally concentrated than the halo mass distribution. For example while the half-mass radius of the dark matter is ∼100 kpc, the radius that contains half of all luminous satellites is only 52 kpc. As is clear from Fig. 5 too, type-1s are much less concentrated than type-2s. Half of all type-1s in Aq-A-L1 are found within 82 kpc, whereas the type-2 half radius is just 18 kpc.

3.5 Satellite number density profile

The number density profile of all surviving subhaloes in Aq-A-L1 has been studied by Springel et al. (2008, see their fig. 11). In particular, the shape of the number density profile was shown to be nearly independent of subhalo mass and well fit by an Einasto profile with parameter values $\alpha = 0.678$ and $r_{-2} = 199$ kpc (see also Ludlow et al. 2009). This is a much shallower central dependence on radius than that of the dark matter, which follows quite well an NFW profile. We show this in Fig. 6, where the grey dotted profile corresponds to all subhaloes, regardless of mass, identified at $z = 0$ in Aq-A-L1. (The thin solid grey line is a best-fitting Einasto profile.) The contributions to this profile from subhaloes with $V_{\rm peak} > 20$ km s^{-1}, and from subhaloes with $10 < V_{\rm peak}/{\rm km\,s^{-1}} < 20$, are also shown with dotted grey lines, in darker tones.

As expected, the number density profile of type-1 luminous satellites (shown with red circles) is similar that of subhaloes with

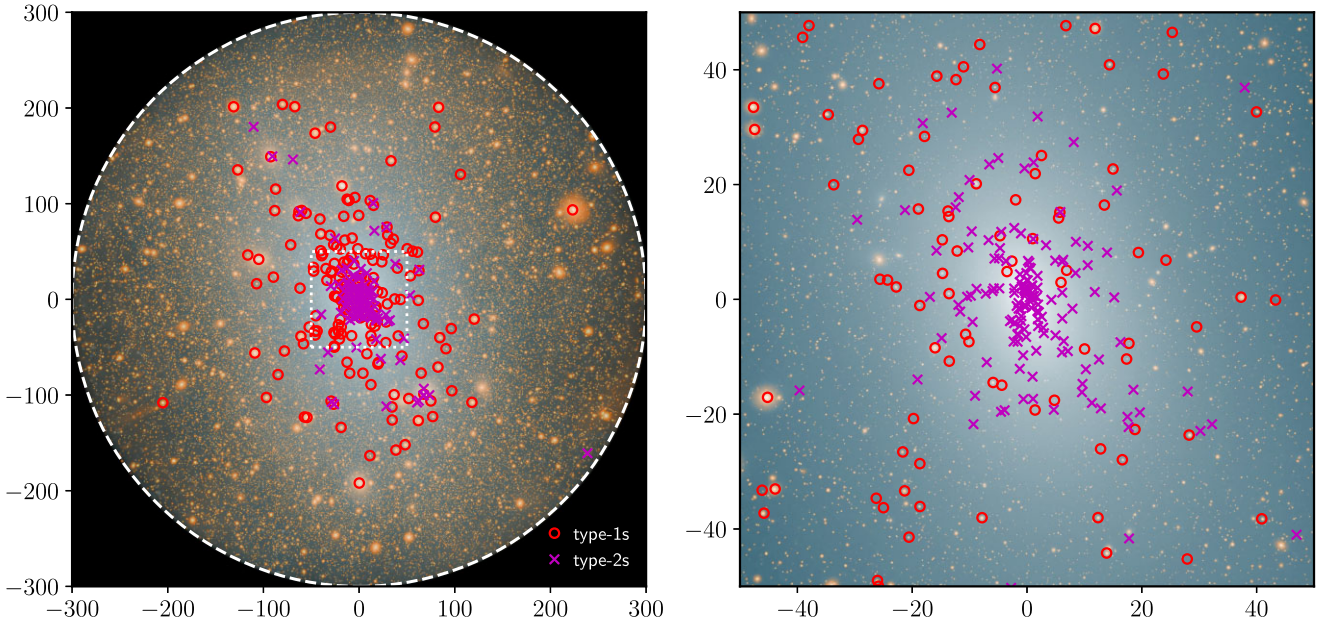

Figure 5. Illustration of the Aq-A-L1 halo and its satellites. The background image shows a density plot where colour intensity correlates with dark matter particle velocity dispersion. Overplotted are type-1 satellite galaxies (open circles) and type-2 satellite galaxies (crosses). A dashed circle marks our 'virial' boundary (300 kpc) within which galaxies are defined as satellites. The right panel is a zoom-in of the inner 50 kpc region around the centre of the Aq-A halo (marked in the left panel with a dotted rectangle).

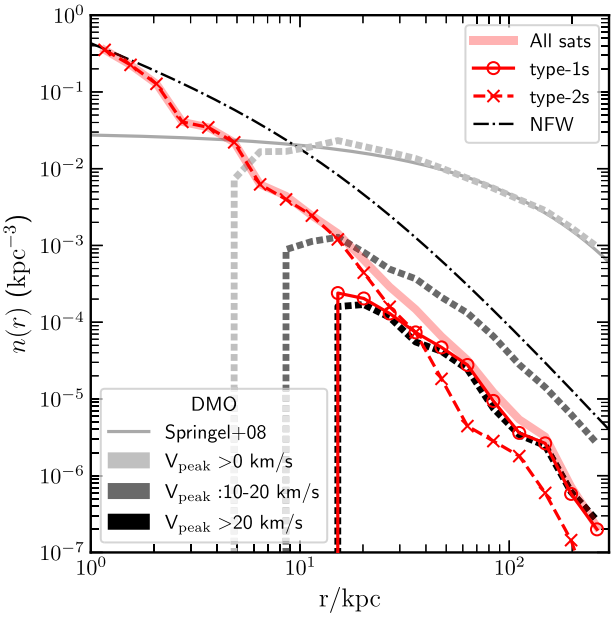

Figure 6. Number density profile of the satellite galaxies of Aq-A-L1. Red crosses correspond to orphan systems, red circles to satellites in surviving subhaloes. The thick pink line is the sum of the two. The dot–dashed curve, for comparison, shows an NFW profile with the same concentration as Aq-A-L1, arbitrarily scaled to match the same central value as the satellite profile. The grey-scale dotted curves show the profiles of subhaloes resolved in the simulation, in bins of $V_{\rm peak}$, as indicated in the legend. The grey line is the best-fitting Einasto profile for all satellites from Springel et al. (2008).

$V_{\rm peak} > 20$ km s^{-1}. Orphan satellites (red crosses), on the other hand, follow a much steeper profile, which crosses the type-1 profile at $r \sim 30$ km s^{-1}. Inside this radius, type-2s dominate, whereas outside type-1s dominate. Note, again that there are no type-1 satellites inside 10 kpc; orphans, on the other hand, are found all the way in, down to ∼1 kpc from the main halo centre. We remind the reader that the Aq-A-L1 simulation does not include the gravitational potential of a central galaxy, nor tidal stripping of stars, which are expected to affect the innermost regions of the satellite number density profile.

In Aq-A-L1, type-1s dominate outside 30 kpc, which implies that surviving subhaloes in *N*-body simulations at this resolution could, in principle, be used to study the luminous satellite population outside that radius. This limiting radius is, however, quite sensitive to resolution: it grows to 69, 102, and 150 kpc for resolution levels 2, 4, and 5, respectively. So far, the highest resolution cosmological hydrodynamical simulations of MW-sized haloes attempted (Sawala et al. 2016; Wetzel et al. 2023; Grand et al. 2024) are comparable to level 2 (i.e. $m_p \approx 10^4\,{\rm M}_\odot$), which means that only satellites in the outer regions of the halo are reliably resolved. A detailed treatment of orphans is therefore critical in order to study the full luminous satellite population of MW-like galaxies.

3.6 Cumulative radial distribution

More detail on the satellite spatial distribution is provided in Fig. 7, where we plot their cumulative radial distribution at $z = 0$. The left-hand panel shows results for simulations of different resolution; the right-hand panel highlights results for the highest resolution simulation and compares them to known MW satellites.

As in Fig. 4, thick solid lines correspond to the full satellite distribution (i.e. type-1s plus type-2s); dashed lines show the radial profile of type-1 satellites only. Few type-1s are present in the innermost regions of the main halo; even for L1 there are no type-1 satellites inside 10 kpc from the centre, a radius that increases as the resolution decreases. In L5, there are no type-1s within 50 kpc from the halo centre.

Type-2s, on the other hand, are heavily biased towards the halo centre, meaning that there is no shortage of satellites expected in

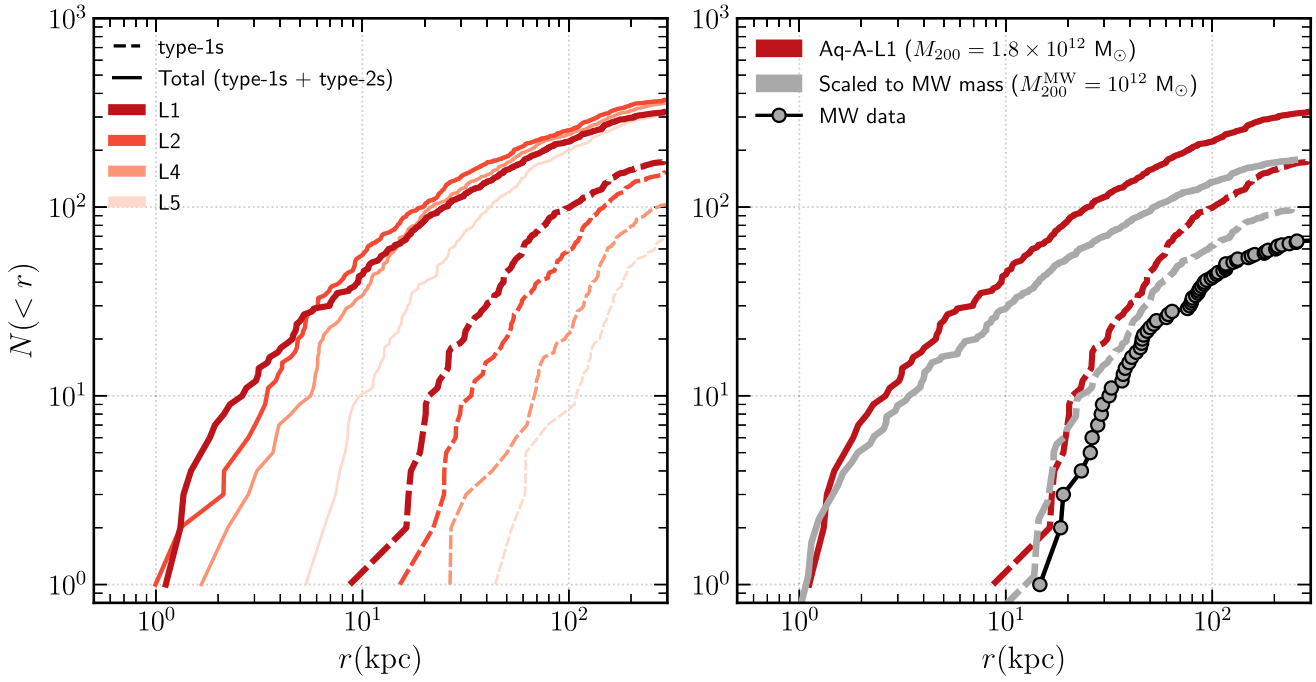

Figure 7. *Left:* cumulative radial distribution of satellite galaxies in Aq-A at $z = 0$. Different colours (and line thickness) correspond to different resolution levels. Dashed lines show results counting only surviving subhaloes (type-1s); solid lines show results for all satellites, i.e. type-1s plus type-2s. *Right:* cumulative radial distribution of Aq-A-L1 satellites (dark red) compared to that of the currently known MW satellites (grey circles). The latter list is likely to be highly incomplete. Since the number of satellites scales roughly with the mass of the host, Aq-A-L1 results from the left panel have been scaled by the estimated total virial mass and radius of the MW, for a more appropriate comparison (grey curves). We use $M_{200}^{\rm MW} = 10^{12}$ M$_\odot$ (Cautun et al. 2020) and the corresponding $r_{200} = 207$ kpc that results from assuming an NFW density profile of average concentration.

the inner regions of a MW-like halo once orphans are accounted for. Within a radius of 10 kpc, we find approximately ∼50 Aq-A-L1 satellites, all of which are type-2s.

Overall, the radial distribution of satellites converges less well than the satellite mass function, suggesting that it is much harder to track subhalo orbits than it is to assign them a stellar mass. Reassuringly, though, results for the two highest resolution simulations (L1 and L2) are practically indistinguishable from each other, suggesting that the radial distribution of all luminous satellites has converged.

Note that the Aq-A-L1 satellite population is quite different from that of known MW satellites, both in total number and in radial distribution. As seen in the right-hand panel of Fig. 7, whereas GALFORM predicts a total number of ∼300 satellites for Aq-A, only ∼66 are known for the MW (grey circles in Fig. 7). Furthermore, GALFORM predicts that half of all satellites are to be found within ∼50 kpc, whereas half of known MW satellites lie outside 80 kpc. No MW satellites have so far been found within 20 kpc from the MW centre, whereas GALFORM predicts roughly 85. Correcting for the roughly ∼ 1.8× higher halo mass of Aq-A than of the MW results in the grey curves in the right-hand panel of Fig. 7, but does not change qualitatively the noted discrepancy.

These differences are not unexpected, since the known population of MW satellites is almost certainly rather incomplete, and their radial distribution is at present poorly constrained (Newton et al. 2018, and references therein). On the other hand, the GALFORM Aq-A-L1 prediction likely overestimates the total number of satellites as well as the central concentration of their radial distribution. Indeed, tidal stripping (enhanced by the presence of the central galaxy) would likely remove a fair fraction of orphans from the population, especially those orbiting in the innermost regions of the main halo.

Although it is difficult to draw strong conclusions without explicitly correcting for these effects, there appears to be, in principle, no insurmountable difficulty in reconciling the known MW satellite population with the Aq-A-L1 results. In particular, there is no shortage of luminous satellites expected in the inner regions of the MW halo; even without considering orphans, the radial distribution of Aq-A-L1 satellites already provides a reasonable match to the MW known satellite radial distribution (see right-hand panel of Fig. 7).

This conclusion is apparently at odds with those of Kelley et al. (2019) and Graus et al. (2019) who argued that too few luminous satellites would remain near the halo centre once the enhanced tidal effects resulting from the growth of the central galaxy are taken into account. This view led these authors to argue that luminous satellites should form in haloes much less massive than the critical mass threshold we have applied here.

Their conclusions, however, were based on the analysis of only type-1 satellites in simulations with lower resolution than ours (their particle mass is 3×10^4 M$_\odot$ compared with 1.7×10^3 M$_\odot$ for Aq-A-L1). As Fig. 7 makes clear, the presence of orphan satellites (which dominate the innermost satellite population) challenges such conclusions. A proper treatment of the tidal evolution and survival of satellites in the innermost regions, as well as improved constraints on the full inventory and radial distribution of the MW satellite population, are needed to make further progress on this problem.

3.7 Orbital properties of Aq-A satellites

We have already discussed in Fig. 1 the orbital properties of two example satellites in Aq-A-L1, a type-1, and a type-2. We now discuss the orbital properties at $z = 0$ of all luminous satellites identified in the simulation.

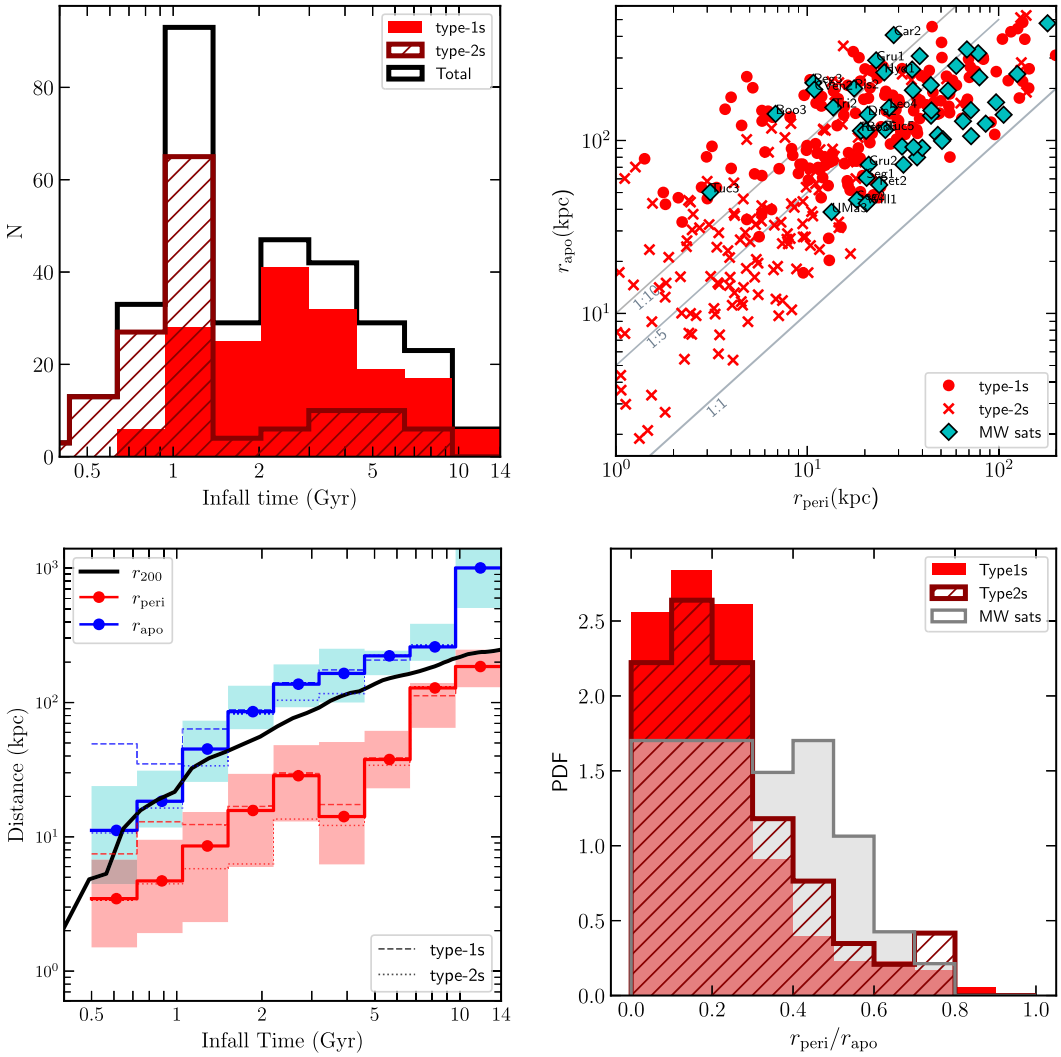

Figure 8. Orbital characteristics of Aq-A-L1 satellites. *Top left:* distribution of infall times for all satellites, including both type-1s and type-2s. *Top right:* pericentric versus apocentric distances at $z = 0$ for type-1s, type-2s, and MW satellites. Thin grey diagonal lines indicate different eccentricities, defined as r_{peri}:r_{apo}. *Bottom left:* median and $\pm 1\sigma$ scatter in pericentric (red line) and apocentric (blue line) distance of satellites in bins of infall time. A black line shows the evolution of the virial radius with time. *Bottom right:* normalized distribution of eccentricities for type-1s, type-2s and MW satellites.

The distribution of infall times for the full satellite sample is shown in the upper left panel of Fig. 8. Type-2s are typically accreted earlier than satellites that survive as bound, resolved subhaloes until $z = 0$. This is because, as in the examples shown in Fig. 1, satellites accreted earlier have, at the present time, smaller apocentric and pericentric radii, as well as shorter orbital times. Unfortunately, computing accurate orbital parameters from the sparse snapshot data stored for Aq-A-L1 is challenging, so we resort to using the $z = 0$ position and velocity of each satellite to integrate backwards in time, keeping the gravitational potential of the main halo fixed. Specifically, the gravitational potential is modelled from the mass distribution of the Aq-A-L1 halo at $z = 0$ assuming spherical symmetry, and we integrate for only 1.5 Gyr back in time. For the mass profile we consider all particles associated with the $z = 0$ Aq-A halo as defined by SUBFIND, reaching out to 640 kpc. Two example orbital integrations are shown by the cyan dashed lines in Fig. 1 (top panels). Pericentre and apocentre distances for each satellite are determined by identifying the radii at which the 3D radial velocity of the satellite changes sign.

These integrations are seen to reproduce the satellite orbits quite well, and may therefore be used to estimate present-day r_{peri} and r_{apo} for all satellites. We show these as a function of infall time in the bottom left panel of Fig. 8. As anticipated when discussing Fig. 1, the apocentric distance of a satellite is, on average, a good measure of the virial radius of the main halo at the time of the satellite's first infall. This explains the offset between the typical infall times of type-1s and type-2s: satellites accreted earlier (generally, orphans) have smaller apocentric and pericentric radii, are subject to much stronger tidal stresses and complete more orbits than systems accreted later, which have a greater chance to survive bound until $z = 0$.

The distribution of infall times is double-peaked, a result that may be traced to a fairly major accretion event which nearly doubled the main halo mass at $t \sim 3$ Gyr. The accreted halo brought its own satellites, which settled on to orbits with higher eccentricity than the average. This may be seen by the dip in pericentric radii in the bottom left panel of Fig. 8, which coincides with the second peak in the infall time distribution.

The bottom left panel of Fig. 8 also indicates that there should be a broad correlation between pericentric and apocentric radii at $z = 0$, which we show in more detail in the top right panel of the figure. Here, solid circles represent type-1s, while crosses depict type-2s. Diagonal grey lines indicate different eccentricities (i.e. different values of the ratio $r_{\rm peri}/r_{\rm apo}$ – 1:1, 1:5, 1:10). The typical eccentricity of Aq-A satellites is roughly 1:5, although the distribution is broad, and contains a number of satellites in highly eccentric, plunging orbits with fairly small pericentres.

As expected from this discussion, the orbits of type-1s and type-2s differ mainly in their apocentric radii. Indeed, few orphans have $r_{\rm apo} > 30$ kpc, and, conversely, there are few, if any, surviving satellites with $r_{\rm apo} < 30$ kpc. This boundary is the radius that separates the region where type-1s dominate over type-2s, as discussed in Section 3.5.

It is interesting to compare these results with current estimates of the orbital parameters of MW satellites for which full kinematic information is available (see Section 2.6 and Appendix A). The MW data are shown in the top right panel of Fig. 8 as cyan diamonds, accompanied by the satellite's name if $r_{\rm peri} < 30$ kpc.

Although most MW satellites overlap in this parameter space with Aq-A-L1 type-1 satellites, there are some notable differences too. Compared to Aq-A-L1, the MW has a dearth of satellites with small pericentric radii, $r_{\rm peri} < 10$ kpc. Such objects are not rare in Aq-A-L1, but there is only one MW satellite with such small pericentre, Tucana 3 (Drlica-Wagner et al. 2015; Shipp et al. 2018; Errani et al. 2023). Although there is still some debate as to whether Tucana 3 is actually a dwarf galaxy or a star cluster, it exhibits prominent tidal tails and is in the process of being tidally disrupted. This is a hint that many satellites with $r_{\rm peri} < 10$ kpc may have been disrupted by tides, a process that is not included in the current study. Likewise, the Aq-A halo potential used in this work lacks the presence of a central baryonic disc, whose additional mass is expected to further influence the simulated satellites' orbits.

There is also the possibility that MW satellites with small $r_{\rm peri}$ could be missing from the current inventory. If these galaxies are very faint (perhaps because they have been heavily stripped), they would be very difficult to identify. One example is the recently detected dwarf galaxy Ursa Major 3, a remarkable system with an estimated stellar mass of only $\sim 14\,{\rm M}_\odot$ (Smith et al. 2024). Although the nature of this object is still debated, its vulnerability to tidal stripping favours its interpretation as a dwarf galaxy (Errani et al. 2024). Objects like this are easy to miss, and call into question how complete our current inventory of faint MW satellites really is.

The bottom right panel in Fig. 8 compares the eccentricity distribution of MW satellites with that of Aq-A-L1. Athough generally consistent, there is some evidence that MW satellites have slightly less eccentric orbits than those in Aq-A-L1. This difference may be influenced by the individual merger histories of the MW and the Aq-A halo, as satellites accreted during past mergers could have settled on to orbits with different eccentricities. None the less, we note that these distributions may be greatly modified once tidal stripping processes are included, so we refrain from drawing strong conclusions from this comparison.

4 SUMMARY AND CONCLUSIONS

We have used the Aquarius suite of dark matter-only zoom-in cosmological simulations to study the abundance, radial distribution, and orbital properties of satellite galaxies in MW-sized haloes formed in a ΛCDM universe. We focus on the Aq-A halo, which was run at various numerical resolutions, enabling an assessment of the sensitivity of our results to numerical limitations. The simulations were coupled with the GALFORM semi-analytical model of galaxy formation to track subhaloes able to form stars which accrete into the main halo at various times. This procedure allows us to track every single luminous satellite expected to form and fall into this halo.

The GALFORM implementation we use assumes that, as discussed by Benitez-Llambay & Frenk (2020), galaxy formation can only take place in dark matter haloes whose mass exceeds a redshift-dependent critical value, which, before reionization, is equal to the mass at which atomic hydrogen cooling becomes effective and, after reionization, is equal to the mass above which gas cannot remain in hydrostatic equilibrium in the presence of a photoionizing background. In practice, this criterion implies that galaxy formation is restricted to haloes with peak circular velocity exceeding 13 km s^{-1}. In terms of $V_{\rm peak}$, the transition between luminous galaxies and 'dark' subhaloes is extremely sharp: 95 per cent of haloes with $V_{\rm peak} = 25$ km s^{-1} are luminous, but only 5 per cent of 15 km s^{-1} haloes harbour luminous galaxies. Below $V_{\rm peak} = 13$ km s^{-1} all haloes remain 'dark', whereas 100 per cent of haloes above 28 km s^{-1} host luminous components.

GALFORM also tracks all luminous subhaloes (i.e. 'satellites') regardless of whether their dark matter component survives the tidal field of the main halo as a self-bound entity. 'Orphan' satellites whose subhaloes have artificially disrupted are an important component, contributing about half of the full, unabridged satellite population predicted by GALFORM. Orphan satellites have typically earlier infall times, smaller pericentric and apocentric radii, and shorter orbital times than those in surviving subhaloes.

Although the inclusion of orphans is a critical improvement of our study over some earlier work, our current implementation neglects the effects of tidal stripping on the stellar component of satellites, as well as the enhanced tidal field due to the assembly of the central galaxy. These two effects are expected to reduce significantly the number of satellites on orbits with small pericentric radii and short orbital times. Therefore, our results are best thought of as the 'maximal' satellite population expected in a MW-sized halo, and not an actual prediction to be directly compared with observational data, particularly in the inner regions of the MW.

Our main findings may be summarized as follows.

(i) A total number of ∼300 satellites within 300 kpc is predicted by our model for Aq-A, a halo with virial mass, $M_{200} = 1.8 \times 10^{12}\,{\rm M}_\odot$, which is likely about twice as massive as that of the MW (Cautun et al. 2020). This is therefore a firm upper limit to the *total* number of MW satellites predicted by our model. This number depends linearly on the assumed MW virial mass, and is sensitive to the assumed reionization redshift and to the details of the evolution of the critical mass, $M_{\rm crit}(z)$. About half these satellites are 'orphans' in our highest resolution simulation, Aq-A-L1, which contains roughly 1 billion dark matter particles within the virial radius of the main halo.

(ii) GALFORM predicts a tight relation between $V_{\rm peak}$ and M_*. Because of the sharp transition in $V_{\rm peak}$ between 'luminous' and 'dark' subhaloes, the satellite stellar mass function is expected to peak at the stellar mass that corresponds to $V_{\rm peak} \approx 15$ km s^{-1}, i.e. $M_* \sim 10^{3.5}\,{\rm M}_\odot$. This implies a sharp downturn in the number of satellites with stellar masses below the peak, a feature of the model that should be verifiable by observations. The differential stellar mass function shows the second peak at $M_* \simeq 10^6\,{\rm M}_\odot$ first noted by Bose et al. (2018) and attributed to the abrupt change in the critical mass threshold caused by reionization. The second peak, however, is less prominent in our study because of the smoother transition in the critical threshold compared to that in Bose et al. (2018).

(iii) Satellites settle on to orbits with apocentric radii that match, on average, the virial radius of the main halo at the time of first infall. The predicted satellite orbits are highly eccentric, with a median pericentre-to-apocentre ratio of 1:5. The model also predicts a substantial fraction of luminous satellites with rather small pericentric radii. The MW has a dearth of satellites on such orbits, a disagreement that may be resolved once tidal stripping of stars is included in GALFORM, a calculation we defer to a future contribution.

(iv) Half of all Aq-A satellites (about 160 objects) are expected to be contained within ∼50 kpc from the main halo centre. Interestingly, only ∼48 of those inhabit subhaloes that are still resolved at $z = 0$ in our highest resolution simulation; the rest are all orphans. There are only 22 MW satellites inside that radius, meaning, that, in principle, there is no obvious difficulty accounting for the observed number of luminous satellites in the inner regions of the MW in our model.

It has recently been argued that the observed number of satellites in the inner regions of the MW is much higher than the number of subhaloes that remain self-bound in cosmological *N*-body simulations (Graus et al. 2019; Kelley et al. 2019). These authors concluded that the MW data can only be reconciled with ΛCDM if luminous galaxies populate subhaloes of extremely low mass, far below the H-cooling limit that determines the critical mass threshold in our study.

We argue that this conclusion is incorrect, mainly as a consequence of ignoring the important contributions of orphans to the simulated satellite population. Indeed, the opposite would seem true: our model predicts far more orphan satellites in the inner regions compared to the relatively small number of known satellites near the centre of the MW, a discrepancy that might be explained by the neglect of tidal disruption of the stellar component of satellites in our model.

Our study underscores the critical need for a proper treatment of the orphan satellite population in order to provide reliable predictions for the full satellite population of the MW down to the ultrafaint regime. This is particularly important since current and upcoming deep observational surveys (e.g. DESI, Vera Rubin Observatory LSST, Roman, *Euclid*) will survey galaxies in our neighbourhood to unprecedented depth.

ACKNOWLEDGEMENTS

We thank the referee for their constructive report which has helped improve this manuscript. ISS and CSF acknowledge support from the European Research Council (ERC) Advanced Investigator grant to CSF, DMIDAS (GA 786910) and from the Science and Technology Facilities Council (ST/P000541/1) and (ST/X001075/1). The simulations for the Aquarius Project were carried out at the Leibniz Computing Centre, Garching, Germany, at the Computing Centre of the Max-Planck Society in Garching, at the Institute for Computational Cosmology in Durham, and on the 'STELLA' supercomputer of the LOFAR experiment at the University of Groningen. This work used the DiRAC@Durham facility managed by the Institute for Computational Cosmology on behalf of the STFC DiRAC HPC Facility (www.dirac.ac.uk). The equipment was funded by BEIS capital funding via STFC capital grants ST/K00042X/1, ST/P002293/1, ST/R002371/1, and ST/S002502/1, Durham University and STFC operations grant ST/R000832/1. DiRAC is part of the National e-Infrastructure. ISS thanks M. Lovell for the background image data for Fig. 5. JFN acknowledges the hospitality of MPA in Garching and DIPC in Donostia-San Sebastián during the completion of this work.

DATA AVAILABILITY

The simulation data underlying this article may be shared upon reasonable request to the Virgo Consortium's steering committee.

REFERENCES

Battaglia G., Taibi S., Thomas G. F., Fritz T. K., 2022, A&A, 657, A54
Bechtol K. et al., 2015, ApJ, 807, 50
Benitez-Llambay A., Frenk C., 2020, MNRAS, 498, 4887
Benson A. J., Lacey C. G., Baugh C. M., Cole S., Frenk C. S., 2002a, MNRAS, 333, 156
Benson A. J., Frenk C. S., Lacey C. G., Baugh C. M., Cole S., 2002b, MNRAS, 333, 177
Bose S., Deason A. J., Frenk C. S., 2018, ApJ, 863, 123
Bose S., Deason A. J., Belokurov V., Frenk C. S., 2020, MNRAS, 495, 743
Bullock J. S., Kravtsov A. V., Weinberg D. H., 2000, ApJ, 539, 517
Callingham T. M. et al., 2019, MNRAS, 484, 5453
Carlsten S. G., Greene J. E., Peter A. H. G., Greco J. P., Beaton R. L., 2020, ApJ, 902, 124
Cautun M. et al., 2020, MNRAS, 494, 4291
Cole S., Aragon-Salamanca A., Frenk C. S., Navarro J. F., Zepf S. E., 1994, MNRAS, 271, 781
Cole S., Lacey C. G., Baugh C. M., Frenk C. S., 2000, MNRAS, 319, 168
Cole S. et al., 2005, MNRAS, 362, 505
Cowley W. I., Baugh C. M., Cole S., Frenk C. S., Lacey C. G., 2018, MNRAS, 474, 2352
Crain R. A. et al., 2015, MNRAS, 450, 1937
Davis M., Efstathiou G., Frenk C. S., White S. D. M., 1985, ApJ, 292, 371
Drlica-Wagner A. et al., 2015, ApJ, 813, 109
Efstathiou G., 1992, MNRAS, 256, 43P
Eilers A.-C., Hogg D. W., Rix H.-W., Ness M. K., 2019, ApJ, 871, 120
Errani R., Navarro J. F., 2021, MNRAS, 505, 18
Errani R., Navarro J. F., Ibata R., Peñarrubia J., 2022, MNRAS, 511, 6001
Errani R., Navarro J. F., Peñarrubia J., Famaey B., Ibata R., 2023, MNRAS, 519, 384
Errani R., Navarro J. F., Smith S. E. T., McConnachie A. W., 2024, ApJ, 965, 20
Fattahi A., Navarro J. F., Frenk C. S., Oman K. A., Sawala T., Schaller M., 2018, MNRAS, 476, 3816
Frenk C. S., White S. D. M., 2012, Annalen der Physik, 524, 507
Gao L., White S. D. M., Jenkins A., Stoehr F., Springel V., 2004, MNRAS, 355, 819
Garrison-Kimmel S. et al., 2019, MNRAS, 487, 1380
Gnedin N. Y., 2000, ApJ, 542, 535
Grand R. J. J., Fragkoudi F., Gómez F. A., Jenkins A., Marinacci F., Pakmor R., Springel V., 2024, MNRAS, 532, 1814
Graus A. S., Bullock J. S., Kelley T., Boylan-Kolchin M., Garrison-Kimmel S., Qi Y., 2019, MNRAS, 488, 4585
Guo Q. et al., 2011, MNRAS, 413, 101
Han J., Cole S., Frenk C. S., Jing Y., 2016, MNRAS, 457, 1208
Hayashi E., Navarro J. F., Taylor J. E., Stadel J., Quinn T., 2003, ApJ, 584, 541
He F., Han J., Li Z., 2025, ApJ, 981, 108
Homma D. et al., 2019, PASJ, 71, 94
Kauffmann G., White S. D. M., Guiderdoni B., 1993, MNRAS, 264, 201
Kelley T., Bullock J. S., Garrison-Kimmel S., Boylan-Kolchin M., Pawlowski M. S., Graus A. S., 2019, MNRAS, 487, 4409
Klypin A., Kravtsov A. V., Valenzuela O., Prada F., 1999, ApJ, 522, 82
Komatsu E. et al., 2009, ApJS, 180, 330
Lacey C. G. et al., 2016, MNRAS, 462, 3854
Li H., Hammer F., Babusiaux C., Pawlowski M. S., Yang Y., Arenou F., Du C., Wang J., 2021, ApJ, 916, 8
Lu S., Frenk C. S., Bose S., Lacey C. G., Cole S., Baugh C. M., Helly J. C., 2024, MNRAS, 536, 1018
Ludlow A. D., Navarro J. F., Springel V., Jenkins A., Frenk C. S., Helmi A., 2009, ApJ, 692, 931

Macciò A. V., Kang X., Fontanot F., Somerville R. S., Koposov S., Monaco P., 2010, MNRAS, 402, 1995
McConnachie A. W., 2012, AJ, 144, 4
McMillan P. J., 2011, MNRAS, 414, 2446
Moore B., Ghigna S., Governato F., Lake G., Quinn T., Stadel J., Tozzi P., 1999, ApJ, 524, L19
Moster B. P., Naab T., White S. D. M., 2013, MNRAS, 428, 3121
Nadler E. O. et al., 2020, ApJ, 893, 48
Navarro J. F., Frenk C. S., White S. D. M., 1996, ApJ, 462, 563
Navarro J. F., Frenk C. S., White S. D. M., 1997, ApJ, 490, 493
Navarro J. F. et al., 2010, MNRAS, 402, 21
Newton O., Cautun M., Jenkins A., Frenk C. S., Helly J. C., 2018, MNRAS, 479, 2853
Okamoto T., Frenk C. S., 2009, MNRAS, 399, L174
Patel E. et al., 2020, ApJ, 893, 121
Pereira-Wilson M., Navarro J. F., Benítez-Llambay A., Santos-Santos I., 2023, MNRAS, 519, 1425
Planck Collaboration VI, 2020, A&A, 641, A6
Sawala T. et al., 2016, MNRAS, 457, 1931
Schaye J. et al., 2015, MNRAS, 446, 521
Schönrich R., Binney J., Dehnen W., 2010, MNRAS, 403, 1829
Shipp N. et al., 2018, ApJ, 862, 114
Simha V., Cole S., 2017, MNRAS, 472, 1392
Simpson C. M., Grand R. J. J., Gómez F. A., Marinacci F., Pakmor R., Springel V., Campbell D. J. R., Frenk C. S., 2018, MNRAS, 478, 548
Smith S. E. T. et al., 2024, ApJ, 961, 92
Somerville R. S., 2002, ApJ, 572, L23
Springel V., White S. D. M., Tormen G., Kauffmann G., 2001, MNRAS, 328, 726
Springel V., Frenk C. S., White S. D. M., 2006, Nature, 440, 1137
Springel V. et al., 2008, MNRAS, 391, 1685
Stadel J., Potter D., Moore B., Diemand J., Madau P., Zemp M., Kuhlen M., Quilis V., 2009, MNRAS, 398, L21
Tegmark M., Silk J., Rees M. J., Blanchard A., Abel T., Palla F., 1997, ApJ, 474, 1
Thoul A. A., Weinberg D. H., 1996, ApJ, 465, 608
van den Bosch F. C., Ogiya G., 2018, MNRAS, 475, 4066
Wang J., Frenk C. S., Navarro J. F., Gao L., Sawala T., 2012, MNRAS, 424, 2715
Wetzel A. et al., 2023, ApJS, 265, 44
White S. D. M., Frenk C. S., 1991, ApJ, 379, 52
White S. D. M., Rees M. J., 1978, MNRAS, 183, 341
Willman B. et al., 2005, ApJ, 626, L85
Zehavi I. et al., 2011, ApJ, 736, 59

APPENDIX A: MW SATELLITE SAMPLES USED FOR COMPARISON

We compare our results to available data for MW satellites, specifically to a sample of 66 satellite candidates located within 300 kpc from the MW centre:

∗Cetus2, **∗Columba1**, ∗DESJ0225 + 0304, **∗Draco2**, ∗Eridanus3, **∗Grus1**, **∗Grus2**, **∗Horologium1**, **∗Horologium2**, ∗Indus1, ∗Indus2, **∗Pegasus3**, **∗Phoenix2**, ∗Pictor1, **∗Reticulum2**, **∗Reticulum3**, **∗Sagittarius2**, **∗Triangulum2**, **∗Tucana3**, **∗Tucana4**, **∗Tucana5**, **Antlia2**, **Aquarius2**, **Bootes1**, **Bootes2**, **Bootes3**, Bootes4, **Bootes5**, **CanesVenatici1**, **CanesVenatici2**, **Carina**, **Carina2**, Carina3, Centaurus1, Cetus3, **ComaBerenices**, **Crater2**, Delve2, **Draco**, Eridanus4, **Fornax**, **Hercules**, **Hydra2**, **Hydrus1**, Leo1, **Leo2**, **Leo4**, **Leo5**, LeoMinor1, **Pegasus4**, Phoenix, Pictor2, **Pisces2**, **Sculptor**, **Segue1**, **Segue2**, **Sextans1**, **Tucana2**, **UrsaMajor1**, **UrsaMajor2**, **UrsaMajor3/UNIONS1**, **UrsaMinor**, Virgo1, **Willman1**, LMC, SMC.

Names preceded by an asterisk indicate objects not spectroscopically confirmed as dwarf galaxies. Names in bold indicate 47 objects with available kinematic data (i.e. line-of-sight velocity and proper motions), for which we derive pericentre and apocentre distances at $z = 0$. These have been computed by integrating backwards the $z = 0$ 3D position and velocity of the object within the Cautun et al. (2020) MW potential, extended beyond 300 kpc assuming an NFW profile with $M_{200} = 10^{12}$ M$_\odot$. Three-dimensional phase-space information has been computed from RA, Dec., $(m - M)$, line-of-sight velocity and proper motion data, as listed in the latest update of McConnachie (2012)'s Nearby Dwarf Galaxy data base (see Section 2.6). We only consider galaxy candidates with derived apocentres smaller than 600 kpc. These are listed in Table A1 and plotted in Fig. 8. (Note we exclude the LMC and SMC from this subsample and from Fig. 8.)

Table A1. Derived $z = 0$ pericentre and apocentre distances for MW satellite candidates with available kinematic data. For details see Section 2.6 and Appendix A. Only galaxy candidates with derived apocentres smaller than 600 kpc are listed below and plotted in Fig. 8.

Name	$r_{\rm peri}$ (kpc)	$r_{\rm apo}$ (kpc)
∗Columba1	180.3	476.1
∗Draco2	20.7	140.7
∗Grus1	22.9	290.6
∗Grus2	21.0	72.4
∗Horologium1	71.8	105.9
∗Horologium2	37.5	79.9
∗Pegasus3	10.8	215.5
∗Phoenix2	78.3	319.6
∗Reticulum2	23.8	55.4
∗Reticulum3	19.1	113.6
∗Sagittarius2	54.4	194.2
∗Triangulum2	13.7	155.1
∗Tucana3	3.1	50.2
∗Tucana4	31.8	72.5
∗Tucana5	25.6	115.1
Antlia2	71.7	149.8
Aquarius2	85.6	125.1
Bootes1	39.9	90.7
Bootes2	38.7	307.7
Bootes3	6.8	142.5
Bootes5	20.3	113.8
CanesVenatici1	60.1	270.3
CanesVenatici2	10.9	196.6
Carina	106.2	140.9
Carina2	28.3	407.0
ComaBerenices	44.4	139.2
Crater2	44.5	149.1
Draco	48.1	107.7
Fornax	97.0	166.1
Hercules	68.3	336.1
Hydra2	35.7	195.2
Hydrus1	25.3	247.5
Leo2	125.2	242.2
Leo4	26.8	154.8
Leo5	44.3	209.1
Pegasus4	31.3	92.2
Pisces2	17.6	200.0
Sculptor	65.1	129.2
Segue1	20.4	60.8
Segue2	18.2	45.3
Sextans1	79.4	231.9
Tucana2	35.3	257.1
UrsaMajor1	51.2	101.6
UrsaMajor2	35.9	91.6
UrsaMajor3/UNIONS1	13.4	38.6
UrsaMinor	50.6	99.4
Willman1	20.4	43.3

APPENDIX B: ABUNDANCE OF SATELLITES AS A FUNCTION OF THE REDSHIFT OF REIONIZATION

In this section, we quantify the differences in the number of satellites expected within 300 kpc of the centre of the Aq-A-L1 host as a function of the assumed redshift of reionization. As explained in Section 2.2, gas cooling and subsequent star formation is allowed in haloes that exceed a critical mass, $M_{\rm crit}$, that evolves with redshift, essentially following the virial mass of a halo in which atomic hydrogen can cool. This evolution shows a discontinuity towards larger masses after reionization, when the gas plasma is heated to $\sim 2 \times 10^4$ K.

The left panel of Fig. B1 illustrates the redshift evolution of $M_{\rm crit}$ for different values of $z_{\rm reion}$. Grey data points show results from our fiducial, $z_{\rm reion} = 6$, case, shown in Fig. 2. The earlier $z_{\rm reion}$, the lower the halo mass at which the jump in $M_{\rm crit}$ occurs, and the lower the number of expected luminous satellites. Indeed, the right panel of Fig. B1 shows that the number of satellites around Aq-A-L1 is heavily

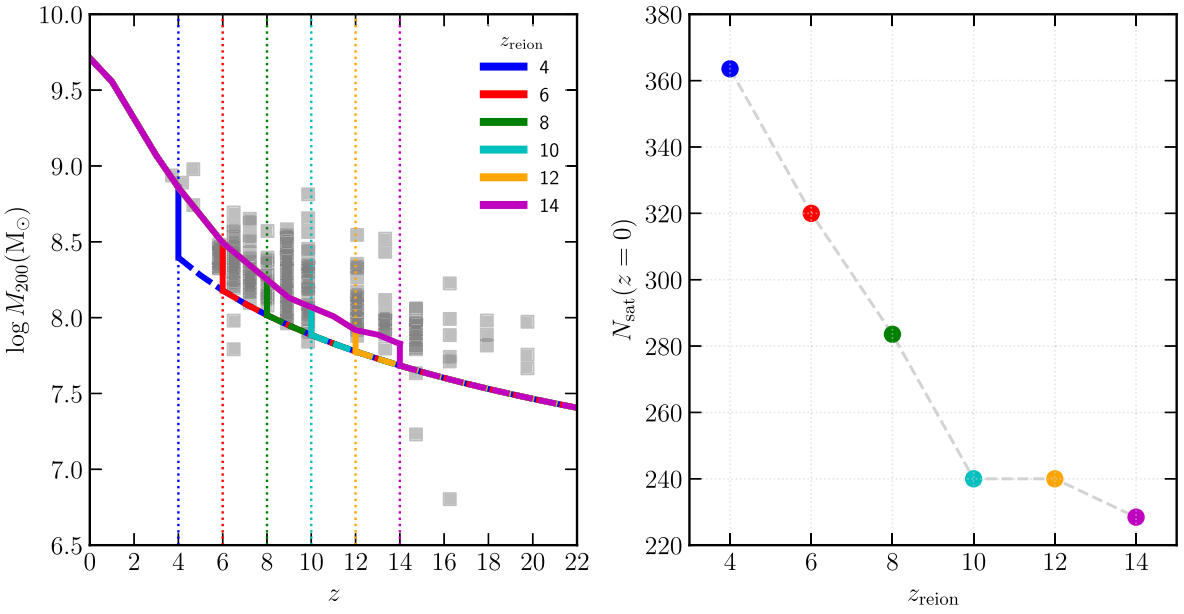

Figure B1. *Left*: as the left panel of Fig. 2, but showing the redshift evolution of the critical mass when assuming different redshifts for reionization, as given in the legend. We refer the reader to Section 2.2 for details of GALFORM modelling. For reference, grey data points show the results for our fiducial $z_{\rm reion} = 6$ model (the same points as in Fig. 2). *Right*: number of satellite galaxies at $z = 0$ predicted by the model assuming different redshifts for reionization. The colour-coding is as in the left panel.

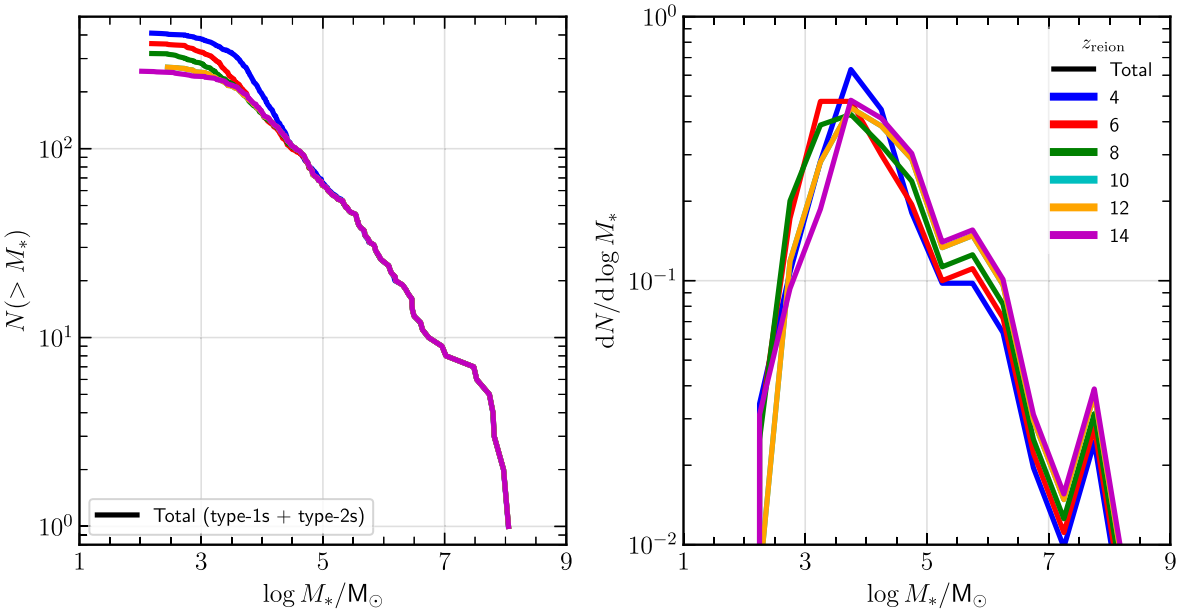

Figure B2. Cumulative (left) and differential (right) satellite luminosity function predicted by GALFORM with different assumed redshifts for reionization, as given in the legend.

dependent on $z_{\rm reion}$: while for $z_{\rm reion} = 6$ we found 320 satellites, for $z_{\rm reion} = 10$ we find 230, roughly ∼30 per cent fewer.[9]

This analysis shows that the number of satellites is not a robust prediction of the model, so long as the redshift of reionization remains uncertain. On the other hand, while the total value of $N_{\rm sat}$ may change when varying $z_{\rm reion}$, the associated differences in the satellite luminosity function affect only the low mass end, $M_{\rm star}<10^{3.5}$ $M_\odot$ (see Fig. B2). Indeed, the shapes of both the cumulative and differential luminosity functions remain essentially unaffected. This is a result of the luminosity function being determined by the underlying subhalo $V_{\rm peak}$ function, which is a fundamental prediction of ΛCDM, combined with the $M_{\rm star} - V_{\rm peak}$ relation, which is a robust prediction of the GALFORM model.

[9]These numbers have been corrected to account for the estimated percentage, ∼ 11 per cent, of 'spurious' low-mass subhaloes in which GALFORM may have mistakenly allowed stars to form due to 'central-swapping' or other merger tree artefacts.

This paper has been typeset from a TEX/LATEX file prepared by the author.